Iterative Monte Carlo analysis of spin-dependent parton distributions

Nobuo Sato, W. Melnitchouk, S. E. Kuhn, J. J. Ethier, and A. Accardi (Jefferson Lab Angular Momentum Collaboration)

Phys. Rev. D **93**, 074005 — Published 5 April 2016

DOI: 10.1103/PhysRevD.93.074005

Iterative Monte Carlo analysis of spin-dependent parton distributions

Nobuo Sato,[1] W. Melnitchouk,[1] S. E. Kuhn,[2] J. J. Ethier,[3] and A. Accardi[4,1]

[1]*Jefferson Lab, Newport News, Virginia 23606, USA*

[2]*Old Dominion University, Norfolk, Virginia 23508, USA*

[3]*College of William and Mary, Williamsburg, Virginia 23187, USA*

[4]*Hampton University, Hampton, Virginia 23668, USA*

Jefferson Lab Angular Momentum (JAM) Collaboration

Abstract

We present a comprehensive new global QCD analysis of polarized inclusive deep-inelastic scattering, including the latest high-precision data on longitudinal and transverse polarization asymmetries from Jefferson Lab and elsewhere. The analysis is performed using a new iterative Monte Carlo fitting technique which generates stable fits to polarized parton distribution functions (PDFs) with statistically rigorous uncertainties. Inclusion of the Jefferson Lab data leads to a reduction in the PDF errors for the valence and sea quarks, as well as in the gluon polarization uncertainty at $x \gtrsim 0.1$. The study also provides the first determination of the flavor-separated twist-3 PDFs and the d_2 moment of the nucleon within a global PDF analysis.

I. INTRODUCTION

The last few years have witnessed tremendous progress in our understanding of the basic decomposition of the proton's spin into its quark and gluon constituent parts, both in terms of moments of spin-dependent parton distribution functions (PDFs) and in their dependence on the momentum fraction x carried by the individual partons [1–4]. Recent data on inclusive jet [5] and pion [6, 7] production in polarized pp collisions at the Relativistic Heavy Ion Collider (RHIC), as well as double spin asymmetries from open charm muonproduction at COMPASS [8], have led to significant improvement in the determination of the polarized gluon distribution at small x [9]. New results on longitudinal single-spin asymmetries in $W^{\pm}$ boson production [10, 11] are also yielding better constraints on the polarization of sea quarks and antiquarks.

In fixed-target deep-inelastic scattering (DIS) experiments, new high-precision data from Jefferson Lab on polarized protons [12–15], deuterons [15, 16] and ^{3}He nuclei [17–19] are yielding a wealth of information on nucleon spin structure at lower energies. As well as improving the constraints on the large-x behavior of polarized PDFs, the new results are also providing new insights into nonperturbative quark-gluon interaction effects through higher twist contributions.

In a previous study [20], the Jefferson Lab Angular Momentum (JAM) Collaboration performed a first analysis of inclusive longitudinal and transverse polarization data down to low values of four-momentum transfer squared Q^2 ($= 1$ GeV^2) and hadronic final state masses squared W^2 ($= 3.5$ GeV^2), systematically taking into account finite-Q^2 and nuclear corrections that are necessary at these kinematics. The increased statistics afforded by the weaker cuts — almost doubling the number of DIS data points — resulted in more reliable determinations of PDFs, particularly at large values of x. In order to avoid dealing with the complications associated with higher twist and nuclear corrections, many PDF analyses impose more stringent cuts on Q^2 and W^2, which unfortunately eliminates much of the data at the highest x values.

Most of the existing phenomenological spin-dependent PDF analyses [21–25] also utilize standard PDF fitting technology, in which single fits are performed assuming a basic parametric form for the PDFs, with the parameters obtained by minimizing the overall χ^2 of the fit. The PDF errors are then typically computed using the Hessian or Lagrange multiplier

methods. A drawback of this approach is that some of the shape parameters do not play a significant role in describing the data, and attempts to fix their values can be rather arbitrary due to correlations among the distributions. In some cases this can lead to overfitting, with the χ^2 per degree of freedom $\chi^2_{\rm dof} \ll 1$. Furthermore, since the χ^2 is a highly non-linear function of the fit parameters, in general there will be many solutions and multiple local minima. In practice, the extensive experience gained over the past two decades with global QCD analyis of leading twist PDFs can be exploited to render relatively stable results through judicious choices for the starting parameters in the χ^2 minimization. One can also tune the number of free parameters in the fits to reduce the number of solutions, even though the solutions can never be guaranteed to be unique. On the other hand, very limited experience exists in fitting parameters for higher twist distributions [20, 26, 27], for which the signals are generally smaller and the kinematic window for maximizing the sensitivity of the fits to their presence is significantly narrower.

Because of these complications, in this work we propose an alternative approach to global PDF analysis, based on a new iterative Monte Carlo (IMC) fitting technique that allows a more robust extraction of both leading and higher twist PDFs, with statistically rigorous PDF uncertainties. The idea behind this new iterative approach is to systematically transform the priors obtained initially from a flat Monte Carlo sampling into posteriors that are distributed consistently with the information contained within the data. Our method shares some similarities with other Monte Carlo approaches, such as that by the NNPDF group [28], who also employ data resampling techniques but use neural networks instead of traditional parametrizations. In particular, we retain the basic parametric form used in standard PDF fitting, but maximally explore the parameter space using Monte Carlo sampling, together with data resampling and cross-validation of the fit. This avoids systematic biases introduced by performing single fits based on an initial guess of the starting PDF parameters, and obviates the necessity of fixing parameters that are not well constrained by data.

To offset the additional expense associated with performing thousands of fits in the IMC approach, we perform all our calculations in Mellin space, in analogy to the methodology adopted by the DSSV group [9, 21]. This requires the implementation of fast evaluation of nuclear smearing [29–31] and target mass corrections (TMCs) [32–36], both of which involve additional integrations in x space. In practice this is achieved by precomputing tables

of moments which can be retrieved during the computation of inverse Mellin transforms. Within this approach the TMCs can be evaluated to all orders in M^2/Q^2, where M is the nucleon mass, instead of just including several low-order terms in the expansion [20].

Another improvement in our new theoretical framework is in the treatment of higher twist contributions to the spin-dependent g_1 and g_2 structure functions. In Ref. [20] the twist-3 part of g_2 was parametrized in terms of a light-cone quark model inspired function of x with 3 parameters, while the twist-4 part of g_1 was fitted using a spline approximation for the x dependence of the $1/Q^2$ term, with knots for the spline at several different x values. Here we adopt for both the twist-3 and twist-4 contributions to g_1 and g_2 the same generic functional form as for the leading twist PDFs, including for the first time a separation into individual u and d flavors (we assume the higher twist contributions, which are more relevant at large x values, to be small in the strange quark sector). In addition, we include TMCs for the twist-3 distributions [33], along with the standard mass corrections for the twist-2 PDFs, as well as Q^2 evolution of the twist-3 functions [37, 38].

As in the previous JAM analysis [20], we use the measured $A_\parallel$ and $A_\perp$ asymmetries, whenever available, instead of the derived A_1 asymmetry or g_1 structure function to avoid uncertainties associated with inconsistent use of spin-averaged structure functions in the extraction of the spin-dependent observables. We include new data sets with high-precision $A_\parallel$ and $A_\perp$ asymmetry measurements at Jefferson Lab from the "eg1b" [14, 16] and "eg1-dvcs" [15] analyses on the proton and deuteron, and new results from the E06-014 experiment on ^{3}He from Hall A [17, 18]. Also included are the most recent A_1 measurements on the proton from COMPASS [39]. To more directly isolate the impact of the new data sets and assess the systematics of our new methodology, we restrict the current analysis to inclusive DIS data only. A full analysis of all data, including semi-inclusive DIS, and inclusive jet and π production in polarized pp collisions, will be presented in a forthcoming publication [40].

In Sec. II of this paper we present a brief review of the basic observables in spin-dependent DIS, and summarize the essential results for the g_1 and g_2 structure functions at finite Q^2, including the effects of target mass, higher twist and nuclear corrections. Our fitting methodology is discussed in Sec. III, where we describe the Mellin space technique and the details of the iterative Monte Carlo procedure. Section IV summarizes the data used in the current fit, and the results of the global analysis are presented in Sec. V. Here we systematically study the stability of the results with respect to cuts on the data for different

minimum values of W^2 and Q^2, in order to establish the extent of the kinematics over which the formalism can provide a reliable description of the data. For the optimal cuts determined by the stability of the moments and the χ^2 values, we present in Sec. V B a detailed comparison of the fitted results with all of the measured polarization asymmetries from the earlier and new experiments.

The impact of the new Jefferson Lab data on the PDFs and their uncertainties is discussed in Sec. V C, including the most precise determination to date of the x dependence of the twist-3 distributions. The extracted twist-2 and twist-3 JAM15 PDFs are presented in Sec. V D, along with the fitted residual higher twist contributions to the structure functions, including the Q^2 dependence of the d_2 moments of the twist-3 distributions. Finally, in Sec. VI we summarize our results and preview future extensions of this work.

II. FORMALISM

In this section we give a brief review of the basic framework for polarized DIS, including the formulas for the measured polarization asymmetries, and the essential results for the spin-dependent structure functions in the operator product expansion of QCD. We also review the unpolarized structure function input that is needed for the extraction of the spin-dependent PDFs from the measured asymmetries.

A. Observables

The inclusive polarized DIS experiments used in this analysis measured cross section asymmetries for lepton scattering from a stationary target with various combinations of target and lepton spin, with the latter always aligned or anti-aligned with the direction of the lepton beam. While some experiments also measured absolute cross section differences [17–19], here we only use the polarization asymmetries.

In the most general case, with the target polarization pointing in a direction given by spherical polar angles θ^* and ϕ^* relative to the direction of the momentum transfer vector $\boldsymbol{q}$, the measured asymmetry is defined as

$$A \;=\; \frac{\sigma^{\downarrow} - \sigma^{\uparrow}}{\sigma^{\downarrow} + \sigma^{\uparrow}} \;=\; \frac{\cos\theta^* \sqrt{1-\epsilon^2}\, A_1 + \sin\theta^* \cos\phi^* \sqrt{2\epsilon(1-\epsilon)}\, A_2}{1 + \epsilon R}, \tag{1}$$

where the arrow $\uparrow$ ($\downarrow$) denotes the spin of the lepton along (opposite to) the beam direction. The variable

$$\epsilon = \frac{2(1-y) - \frac{1}{2}\gamma^2 y^2}{1 + (1-y)^2 + \frac{1}{2}\gamma^2 y^2} \tag{2}$$

is the ratio of longitudinal to transverse photon polarizations, where $y = \nu/E$ is the fractional energy transfer from the lepton in the target rest frame, $\gamma^2 = 4M^2x^2/Q^2$, and $x = Q^2/2M\nu$ is the Bjorken scaling variable. In Eq. (1), A_1 and A_2 are the virtual photoproduction asymmetries, and $R = \sigma_L/\sigma_T$ is the ratio of the longitudinal to transverse virtual photoproduction cross sections. For the case where the target polarization is either along ($\Uparrow$) or perpendicular to ($\Rightarrow$) the beam direction, the general expression for the asymmetry in Eq. (1) reduces to the logitudinal and transverse asymmetries, defined by

$$A_\parallel = \frac{\sigma^{\downarrow\Uparrow} - \sigma^{\uparrow\Uparrow}}{\sigma^{\downarrow\Uparrow} + \sigma^{\uparrow\Uparrow}} = D(A_1 + \eta A_2), \tag{3}$$

$$A_\perp = \frac{\sigma^{\downarrow\Rightarrow} - \sigma^{\uparrow\Rightarrow}}{\sigma^{\downarrow\Rightarrow} + \sigma^{\uparrow\Rightarrow}} = d(A_2 - \zeta A_1), \tag{4}$$

where the kinematical variables here are given by

$$\begin{aligned} D &= \frac{y(2-y)(2+\gamma^2 y)}{2(1+\gamma^2)y^2 + (4(1-y) - \gamma^2 y^2)(1+R)}, \\ d &= \frac{\sqrt{4(1-y) - \gamma^2 y^2}}{2-y} D, \\ \eta &= \gamma \frac{4(1-y) - \gamma^2 y^2}{(2-y)(2+\gamma^2 y)}, \qquad \zeta = \gamma \frac{2-y}{2+\gamma^2 y}. \end{aligned} \tag{5}$$

These definitions for the asymmetries are consistent with the ones commonly found in the literature (in which the spin of the lepton is fixed but that of the target is flipped), if one parity-violating effects can be neglected. The virtual photoproduction asymmetries can be expressed as ratios of spin-dependent (g_1 and g_2) and spin-averaged (F_1 and F_2) structure functions,

$$A_1 = \frac{(g_1 - \gamma^2 g_2)}{F_1}, \qquad A_2 = \gamma \frac{(g_1 + g_2)}{F_1}, \tag{6}$$

with the ratio R given in terms of the spin-averaged structure functions by

$$R = \frac{(1+\gamma^2)F_2 - 2xF_1}{2xF_1}. \tag{7}$$

At large values of Q^2, the variables η and ζ in Eq. (5) vanish, and the longitudinal and transverse asymmetries become proportional to A_1 and A_2, respectively. In this case the polarization asymmetry $A_1 \approx g_1/F_1$, and has a simple interpretation in terms of parton distributions, as we discuss next.

B. Structure functions in QCD

In the leading twist (twist $\tau = 2$) approximation the g_1 structure function can be computed in terms of spin-dependent PDFs,

$$g_1^{(\tau 2)}(x, Q^2) = \frac{1}{2} \sum_q e_q^2 \left[(\Delta C_q \otimes \Delta q^+)(x, Q^2) + \ (\Delta C_g \otimes \Delta g)(x, Q^2) \right], \tag{8}$$

where $\Delta q^+ = \Delta q + \Delta \bar{q}$ is the sum of the quark and antiquark PDFs, Δg is the gluon PDF, and ΔC_q and ΔC_g are the respective hard scattering coefficients, calculable in perturbative QCD. In this analysis we use the hard scattering coefficients computed to next-to-leading order (NLO) accuracy, as is standard in all global spin PDF analyses. The symbol "$\otimes$" denotes the convolution integral, $(\Delta C \otimes \Delta f)(x) = \int_x^1 (dz/z) \Delta C(z) \Delta f(x/z)$. In the leading twist approximation, the g_2 structure function is given in terms of the twist-2 component of g_1 via the Wandzura-Wilczek relation [41],

$$g_2^{(\tau 2)}(x, Q^2) = -g_1^{(\tau 2)}(x, Q^2) + \int_x^1 \frac{dz}{z} g_1^{(\tau 2)}(z, Q^2). \tag{9}$$

Defining the N-th moments of the $g_{1,2}$ structure functions as

$$\boldsymbol{g}_{1,2}(N, Q^2) = \int_0^1 dx \, x^{N-1} \, g_{1,2}(x, Q^2), \tag{10}$$

one finds that the lowest ($N = 1$) moment of $g_2^{(\tau 2)}$ satisfies the Burkhardt-Cottingham (BC) sum rule [42],

$$\boldsymbol{g}_2^{(\tau 2)}(1, Q^2) = 0. \tag{11}$$

While these results are, strictly speaking, valid in the Bjorken limit ($Q^2 \to \infty$, x fixed), at finite values of Q^2, power-suppressed [$\mathcal{O}(1/Q^2)$] corrections to the structure functions can make important contributions in some kinematic regions. The simplest of these are the target mass corrections, which in the operator product expansion are associated with matrix elements of twist-2 operators with insertions of covariant derivatives [43]. These do not alter the twist classification, but lead to corrections to the structure functions that scale with the Nachtmann variable ξ, where [43, 44]

$$\xi = \frac{2x}{1 + \rho}, \qquad \rho^2 = 1 + \gamma^2. \tag{12}$$

For the target mass corrected g_1 structure function, one has [32, 33]

$$g_1^{(\tau 2+\mathrm{TMC})}(x,Q^2) = \frac{x}{\xi\rho^3}\, g_1^{(\tau 2)}(\xi,Q^2) + \frac{(\rho^2-1)}{\rho^4}\int_\xi^1 \frac{dz}{z}\left[\frac{(x+\xi)}{\xi} - \frac{(3-\rho^2)}{2\rho}\ln\frac{z}{\xi}\right] g_1^{(\tau 2)}(z,Q^2), \tag{13}$$

while the g_2 target mass corrected structure function is given by

$$g_2^{(\tau 2+\mathrm{TMC})}(x,Q^2) = -\frac{x}{\xi\rho^3}\, g_1^{(\tau 2)}(\xi,Q^2) + \frac{1}{\rho^4}\int_\xi^1 \frac{dz}{z}\left[\frac{x}{\xi} - (\rho^2-1) + \frac{3(\rho^2-1)}{2\rho}\ln\frac{z}{\xi}\right] g_1^{(\tau 2)}(z,Q^2). \tag{14}$$

Note that in the presence of TMCs, the finite-Q^2 structure functions in Eqs. (13) and (14) are nonzero at $x = 1$, vanishing only in the $\xi \to 1$ limit. The nonvanishing of the target mass corrected structure functions at $x = 1$ is usually referred to as the "threshold problem" [45–47], and has been discussed at length in the literature [48–52]. In practice, the kinematics where this problem becomes relevant are restricted to the nucleon resonance region, at values of W^2 far below those where a perturbative QCD analysis is applicable.

The Q^2 dependence of the massless limit functions $g_{1,2}^{(\tau 2)}$ on the right hand sides of Eqs. (13) and (14) is due to the perturbative QCD evolution of the twist-2 distributions themselves. Clearly in the large-Q^2 limit, when $\rho \to 1$ and $\xi \to x$, Eq. (14) reduces to the Wandzura-Wilczek relation, Eq. (9). However, even in the presence of TMCs, Eq. (9) with $g_{1,2}^{(\tau 2)}$ replaced by $g_{1,2}^{(\tau 2+\mathrm{TMC})}$ is still satisfied, provided the integration of the second term is extended to $1/(1 - M^2/Q^2)$, which corresponds to evaluating the target mass corrected structure functions in Eqs. (13) and (14) up to $\xi = 1$. Moreover, the BC sum rule is also satisfied for the target mass corrected structure function $g_2^{(\tau 2+\mathrm{TMC})}$.

In addition to the kinematical TMCs, structure functions in the operator product expansion receive contributions also from higher twist terms which are associated with matrix elements of quark-gluon or multi-quark operators. As with the TMCs, these vanish at large Q^2, but at low Q^2 values ($Q^2 \sim 1$ GeV^2) can play an important role in DIS. Of course, if Q^2 is too small, then the expansion in $1/Q^2$ will not be convergent; however, at low, but not too low, Q^2 values there will be a window in which the higher twist contributions themselves can be extracted from data [53–56]. Keeping only the higher twist terms that contribute at the lowest order in $\sim 1/Q^2$, we use the following expansion for the structure functions,

$$g_1 = g_1^{(\tau 2)} + g_1^{(\tau 3)} + g_1^{(\tau 4)}, \tag{15}$$

$$g_2 = g_2^{(\tau 2)} + g_2^{(\tau 3)}, \tag{16}$$

where, with the exception of the twist $\tau = 4$ term, each of the other ($\tau = 2$ and 3) contributions implicitly contains TMCs. In particular, for the twist-3 part of the g_1 structure function, one has [33]

$$g_1^{(\tau 3+\mathrm{TMC})}(x,Q^2) = \frac{(\rho^2-1)}{\rho^3}\, D(\xi,Q^2) - \frac{(\rho^2-1)}{\rho^4}\int_\xi^1 \frac{dz}{z}\left[3 - \frac{(3-\rho^2)}{\rho}\ln\frac{z}{\xi}\right] D(z,Q^2), \quad (17)$$

where the function D is expressed in terms of twist-3 parton distributions,

$$D(x,Q^2) = \sum_q e_q^2 D_q(x,Q^2). \quad (18)$$

Similarly, for the target mass corrected twist-3 part of the g_2 structure function one has [33]

$$g_2^{(\tau 3+\mathrm{TMC})}(x,Q^2) = \frac{1}{\rho^3}\, D(\xi,Q^2) - \frac{1}{\rho^4}\int_\xi^1 \frac{dz}{z}\left[3 - 2\rho^2 + \frac{3(\rho^2-1)}{\rho}\ln\frac{z}{\xi}\right] D(z,Q^2). \quad (19)$$

Note that at large Q^2 the twist-3 part of g_1 vanishes, since nonzero values of $g_1^{(\tau 3+\mathrm{TMC})}$ arise only from target mass effects. On the other hand, the twist-3 part of the g_2 structure function remains nonzero even in the $M^2/Q^2 \to 0$ limit (in which $\rho \to 1$ and $\xi \to x$), where it is given by an expression similar to the Wandzura-Wilczek relation for the twist-2 part of g_2,

$$g_2^{(\tau 3)}(x,Q^2) = D(x,Q^2) - \int_x^1 \frac{dz}{z} D(z,Q^2). \quad (20)$$

In this limit, one can see by inspection that the twist-3 component of g_2 also satisfies the BC sum rule (11), $\boldsymbol{g}_2^{(\tau 3)}(1,Q^2) = 0$. As in the case of the twist-2 contribution, the BC sum rule also holds for the twist-3 part in the presence of TMCs.

In Eqs. (19) and (20) the Q^2 dependence of the twist-3 function D is generated perturbatively [37, 38], and in our analysis we use the large-N_c approximation to describe the evolution of the moments $\boldsymbol{D}(N,Q^2)$ of the twist-3 functions in Mellin space,

$$\boldsymbol{D}(N,Q^2) \approx \left(\frac{\alpha_S(Q^2)}{\alpha_S(Q_0^2)}\right)^{\widetilde{\gamma}} \boldsymbol{D}(N,Q_0^2), \quad (21)$$

where the moments $\boldsymbol{D}(N,Q^2)$ are defined analogously to Eq. (10). Here α_S is the strong running coupling, and the evolution from the initial scale Q_0^2 is governed by the anomalous dimension

$$\widetilde{\gamma} = \frac{1}{(11-\frac{2}{3}N_f)}\left(\psi(0,N) + \gamma_E - \frac{1}{4} + \frac{1}{2N}\right), \quad (22)$$

where $\psi(0,N)$ is the polygamma function of order 0, γ_E is the Euler-Mascheroni constant, and N_f is the number of active flavors.

Of particular interest is the d_2 integral, which is defined by a combination of $N=3$ moments of g_1 and g_2 [57],

$$d_2(Q^2) = 2\boldsymbol{g}_1(3,Q^2) + 3\boldsymbol{g}_2(3,Q^2). \tag{23}$$

From Eq. (9) one observes that the twist-2 contributions to d_2 vanish identically, so that the leading contributions to d_2 arise at the twist-3 level. In terms of moments of the D_q distributions in Eq. (18), the leading (twist-3) part of d_2 is given by

$$d_2^{(\tau 3)}(Q^2) = \sum_q e_q^2\, \boldsymbol{D}_q(3,Q^2). \tag{24}$$

Physically, d_2 is related to matrix elements describing the nucleon's "color polarizability" [58–60] or the "transverse color force" [61] acting on quarks.

Finally, for the residual twist-4 and higher contributions to the g_1 structure function in Eq. (15) we use an effective hadronic level parametrization,

$$g_1^{(\tau 4)}(x,Q^2) = \frac{H(x,Q^2)}{Q^2}, \tag{25}$$

where H is in general a function of x and Q^2. Since the function H will be fitted phenomenologically, and treated as a background to the twist-2 and twist-3 contributions that are the primary focus of our analysis, we do not include target mass or Q^2 evolution corrections in H. For completeness, we also define the third moment of H by

$$h(Q^2) = \boldsymbol{H}(3,Q^2), \tag{26}$$

where the Mellin transform $\boldsymbol{H}(N,Q^2)$ is defined as in Eq. (10). In summary then, our analysis of the g_1 and g_2 structure functions will involve the twist-2 polarized PDFs Δq and Δg, the twist-3 distributions D_q, and the residual higher twist functions $H_{p,n}$ for the proton and neutron.

C. Spin-averaged structure functions

The extraction of spin-dependent PDFs from the polarization asymmetries in Sec. II A requires information on the spin-averaged structure functions in the denominators of the asymmetries. Ideally, the unpolarized and polarized structure functions should be determined in a simultaneous fit to all DIS and other high energy scattering data, to take into account the possible influence of the spin-dependent data on the unpolarized observables. Such correlations are likely to be small, however, compared with the current uncertainties on the asymmetries, and are neglected in all existing global PDF analyses.

In the JAM15 analysis we use the CJ12 global fit [62] of the spin-averaged PDFs, taking advantage of the similarity in the DIS kinematic cuts employed in both analyses, and the theoretical treatment of target mass, higher twist and nuclear corrections. The fitted CJ12 PDF parameters are then used to evolve the unpolarized distributions and compute the spin-averaged structure functions at the needed Q^2 scale. In the CJ12 fit the strong coupling constant is computed using an approximate analytical form, while the JAM15 analysis solves for α_S numerically. To avoid spurious numerical effects in the calculation of the unpolarized structure functions from a mismatch in the Q^2 evolution [63], the CJ12 PDFs are refitted utilizing the same numerical evolution routine adopted in the JAM framework, and benchmarked against the natively calculated CJ12 observables.

The CJ12 analysis [62] provided NLO fits to the leading twist PDFs, as well as the twist-4 contributions to the F_2 structure function. On the other hand, the polarization asymmetries in Eq. (6) depend on the F_1 structure function, which can be written as a combination of F_2 and the ratio R in Eq. (7). Following Alekhin *et al.* [64], who found very small higher twist contributions to R over the entire x range of the available DIS data, we set the twist-4 component of R to zero. This allows the twist-4 part of F_1 to be computed as $F_1^{(\tau 4)} = F_1^{(\tau 2)}(1 + C_{\rm HT}(x)/Q^2)$, with the higher twist $C_{\rm HT}(x)$ coefficient function taken from the CJ12 fit for F_2 [62].

For the TMCs, the CJ12 fit utilized the collinear factorization formalism of Ref. [52] rather than the operator product approach adopted here. The differences, however, between the two approaches have been shown [65] to be minimal in the x and Q^2 region covered by the spin-dependent data.

III. METHODOLOGY

Having defined the polarization observables and structure functions necessary for a QCD-based analysis, in this section we outline our methodology for fitting the spin-dependent PDFs to the inclusive DIS data. We perform our analysis in moment space, which requires efficient computation of inverse Mellin transforms, but has the advantage of significantly shorter fitting times compared with x-space based analyses [21]. Following this we describe the novel aspect of our analysis, namely the iterative Monte Carlo technique.

A. Mellin space techniques

Calculation of the asymmetries and structure functions discussed in the previous section involves at least two integrations for both twist-2 and twist-3 observables. For instance, the computation of the target mass corrected $g_1^{(\tau 2+\mathrm{TMC})}$ structure function involves a convolution of the spin-dependent PDFs with the hard coefficient functions, as well as additional integrations from the TMCs. The numerical complexity of the problem further increases as one considers the Q^2 evolution equations for the twist-2 distributions.

It turns out, however, that the computational burden can be significantly reduced through the use of Mellin space techniques [21]. Firstly, the Q^2 evolution equations in Mellin space are ordinary coupled differential equations, which are simpler and faster to solve compared with the corresponding integro-differential equations in x-space. Secondly, using the techniques developed by Stratmann and Vogelsang [66], it is possible to cast the various multidimensional integrations in terms of precomputed quantities, thereby significantly decreasing the computational time needed for the observables in the global fits.

To illustrate the technique, consider the case of $g_1^{(\tau 2+\mathrm{TMC})}$ in Eq. (13). For this we write the leading twist part of g_1 in the Mellin representation as

$$g_1^{(\tau 2)}(x,Q^2) = \frac{1}{2\pi i}\int dN\, x^{-N} \boldsymbol{g}_1^{(\tau 2)}(N,Q^2), \tag{27}$$

where the moments $\boldsymbol{g}_1^{(\tau 2)}(N,Q^2)$ are defined in Eq. (10), and inserting this into the target

mass corrected expression in Eq. (13) gives

$$g_1^{(\tau 2+\mathrm{TMC})}(x,Q^2) = \frac{1}{2\pi i}\int dN\, \boldsymbol{g}_1^{(\tau 2)}(N,Q^2) \times\left\{\frac{x}{\xi^{N+1}\rho^3}+\frac{(\rho^2-1)}{\rho^4}\int_\xi^1 \frac{dz}{z^{N+1}}\left[\frac{(x+\xi)}{\xi}-\frac{(3-\rho^2)}{2\rho}\ln\frac{z}{\xi}\right]\right\}. \quad (28)$$

To simplify the notation we define the quantity in the braces by $\mathcal{M}(x,Q^2,N)\equiv\{\cdots\}$ in Eq. (28), which is a function of x, Q^2 and N. Crucially, $\mathcal{M}(x,Q^2,N)$ is independent of the parameters to be fitted, which are confined entirely in the $\boldsymbol{g}_1^{(\tau 2)}$ moments. Furthermore, the moments $\boldsymbol{g}_1^{(\tau 2)}$ are simple products of the moments of the hard coefficients and the spin-dependent PDFs, so that Eq. (28) can be recast in the form

$$g_1^{(\tau 2+\mathrm{TMC})}(x,Q^2) \;=\; \frac{1}{2\pi i}\int dN\,\mathcal{M}(x,Q^2,N) \times\frac{1}{2}\sum_q e_q^2\Big[\Delta\boldsymbol{C}_q(N)\Delta\boldsymbol{q}^+(N,Q^2)+\Delta\boldsymbol{C}_g(N)\Delta\boldsymbol{g}(N,Q^2)\Big]. \quad (29)$$

Here the integration over N is performed numerically in the standard way by using a contour in the complex plane parametrized as $N=c+z\,e^{i\phi}$. The contour crosses the real axis at c, which is set to the right of the rightmost pole of the integrand, and ϕ is set equal to $3\pi/4$ to guarantee convergence of the integral. Using the symmetry of the integrand with respect to the real axis one can then write Eq. (29) as

$$g_1^{(\tau 2+\mathrm{TMC})}(x,Q^2) \;=\; \frac{1}{\pi}\int_0^\infty dz\,\mathrm{Im}\Big\{e^{i\phi}\mathcal{M}(x,Q^2,N) \times\frac{1}{2}\sum_q e_q^2\Big[\Delta\boldsymbol{C}_q(N)\Delta\boldsymbol{q}^+(N,Q^2)+\Delta\boldsymbol{C}_g(N)\Delta\boldsymbol{g}(N,Q^2)\Big]\Big\}. \quad (30)$$

Expressing the integration over z in terms of a Gaussian quadrature sum with Gaussian weights w_i [63], one can approximate

$$g_1^{(\tau 2+\mathrm{TMC})}(x,Q^2) \;\simeq\; \frac{1}{\pi}\sum_i w_i\,\mathrm{Im}\Big\{e^{i\phi}\mathcal{M}(x,Q^2,N_i) \times\frac{1}{2}\sum_q e_q^2\Big[\Delta\boldsymbol{C}_q(N_i)\Delta\boldsymbol{q}^+(N_i,Q^2)+\Delta\boldsymbol{C}_g(N_i)\Delta\boldsymbol{g}(N_i,Q^2)\Big]\Big\}, \quad (31)$$

where now all the unknown quantities to be fitted (namely, Δq^+ and Δg) decouple from the multidimensional integrations which are contained inside $\mathcal{M}(x,Q^2,N_i)$. The latter can be computed prior to the fit such that the observable becomes a simple finite sum over the complex moments $N_i=c+z_i\,e^{i\phi}$.

Potentially similar complications arise with the implementation of the nuclear smearing corrections, in which the nuclear (deuteron and ^{3}He) structure functions are expressed as convolutions of the nuclear smearing functions and bound nucleon structure functions [29–31],

$$g_i^A(x,Q^2) = \sum_{\tau=p,n} \int_x^A \frac{dz}{z} f_{ij}^{\tau/A}(z,\rho)\, g_j^\tau\left(\frac{x}{z},Q^2\right), \tag{32}$$

where the smearing function $f_{ij}^{\tau/A}(z,\rho)$ represents the spin-depenent light-cone momentum distribution of nucleon $\tau = p$ or n in the nucleus A, and g_j^τ is the nucleon structure function ($i,j = 1,2$). In principle the bound nucleon structure functions can also depend on the degree to which the nucleons are off-shell, but in practice these effects are likely to be smaller than the current experimental uncertainties on the polarization data [31]. At large Q^2 the smearing functions $f_{ij}^{\tau/A}$ are steeply peaked around $z = 1$ and are independent of Q^2, but acquire Q^2 (or rather ρ) dependence at finite Q^2 values [29, 30]. In moment space the nuclear structure functions can also be expressed in the compact form

$$g_i^A(x,Q^2) = \sum_{\tau=p,n} \frac{1}{2\pi i} \int dN\, \mathcal{M}_{ij}^{\tau/A}(x,Q^2,N)\, \boldsymbol{g}_j^\tau(N,Q^2), \tag{33}$$

where the smeared nuclear kinematic factor is given by

$$\mathcal{M}_{ij}^{\tau/A}(x,Q^2,N) = \int_0^1 \frac{dz}{z} f_{ij}^{\tau/A}(z,\rho)\, \mathcal{M}\left(\frac{x}{z},Q^2,N\right), \tag{34}$$

which now contains both nuclear and target mass corrections. As for the TMC implementation in Eqs. (29)–(31), the factors $\mathcal{M}_{ij}^{\tau/A}$ can be precomputed, allowing a more efficient evaluation of the nuclear structure functions during the fitting procedure.

B. PDF parametrization and errors

For the generic parametrization of the spin-dependent PDFs, as well as the twist-3 distributions D_q and the twist-4 functions $H_{p,n}$, we choose the standard functional form

$$f(x,Q_0^2) = \mathcal{N}\, x^a (1-x)^b (1 + c\sqrt{x} + d\,x) \tag{35}$$

at the input scale Q_0^2, in terms of the four shape parameters a, b, c and d, and the normalization $\mathcal{N}$. In Mellin space the moments of f are defined as in Eq. (10) and can be expressed

analytically using the beta function B,

$$\boldsymbol{f}(N, Q_0^2) \;=\; \mathcal{N}\Big[B(N+a, b+1) + c\, B(N+a, b+3/2) + d\, B(N+a, b+2)\Big]. \tag{36}$$

Since the present analysis only considers inclusive DIS data, we attempt to fit only the PDFs Δu^+, Δd^+, Δs^+ and Δg, and the higher twist distributions D_u, D_d, H_p and H_n. For the polarized sea quark distributions we follow some previous PDF analyses [22] in assuming a flavor symmetric sea,

$$\Delta\bar{s}(x, Q^2) = \Delta\bar{u}(x, Q^2) = \Delta\bar{d}(x, Q^2) = \frac{1}{2}\Delta s^+(x, Q^2). \tag{37}$$

Additional constraints on the moments of the PDFs are provided by the weak neutron and hyperon decay constants,

$$\Delta\boldsymbol{u}^+(1, Q^2) - \Delta\boldsymbol{d}^+(1, Q^2) = g_A, \tag{38}$$

$$\Delta\boldsymbol{u}^+(1, Q^2) + \Delta\boldsymbol{d}^+(1, Q^2) - 2\Delta\boldsymbol{s}^+(1, Q^2) = a_8, \tag{39}$$

where the moments $\Delta\boldsymbol{q}^+(1, Q^2)$ are defined as in Eq. (36), and the triplet and octet axial vector charges are given by $g_A = 1.269(3)$ and $a_8 = 0.586(31)$, respectively. Note that the nonsinglet combinations in Eqs. (38) and (39) are independent of Q^2, whereas the quark singlet combination,

$$\Delta\Sigma(Q^2) = \sum_q \Delta\boldsymbol{q}^+(1, Q^2), \tag{40}$$

as well as the gluon moment $\Delta G(Q^2) = \Delta\boldsymbol{g}(1, Q^2)$, are scale dependent.

The fit parameters are determined by minimizing the χ^2 function, which we define as

$$\chi^2 = \sum_e \left[\sum_i \left(\frac{\mathcal{D}_i^{(e)} N_i^{(e)} - T_i^{(e)}}{\alpha_i^{(e)} N_i^{(e)}} \right)^2 + \sum_k \left(r_k^{(e)} \right)^2 \right], \tag{41}$$

where $\mathcal{D}_i^{(e)}$ is the measured value of the observable for the data point i from the experimental data set e, with $T_i^{(e)}$ the corresponding theoretical value; $\alpha_i^{(e)}$ represents the uncorrelated statistical and systematic uncertainties added in quadrature. To account for correlated (point-to-point) systematic uncertainties $\beta_{k,i}^{(e)}$ in each experiment e, we introduce normalization factors of the form

$$N_i^{(e)} = 1 - \frac{1}{\mathcal{D}_i^{(e)}} \sum_k r_k^{(e)} \beta_{k,i}^{(e)}, \tag{42}$$

parametrized in terms of "nuisance parameters" $r_k^{(e)}$. To control the size of the normalization factors, a penalty term is introduced in Eq. (41) as a quadrature sum of the $r_k^{(e)}$ values, such that the fitted normalization factors resemble Gaussian statistics.

Note that the normalization factors $N_i^{(e)}$ rescale both the data values $\mathcal{D}_i^{(e)}$ and the uncorrelated (statistical and point-to-point systematic) uncertainties $\alpha_i^{(e)}$. This accounts for the fact that overall experimental scale factors, such as the beam and target polarizations and dilution factors, multiply both the data values and (in particular) their statistical errors (which dominate $\alpha_i^{(e)}$) in the same way. Moreover, considering only the rescaling of $\mathcal{D}_i^{(e)}$ would lead to a strong downward bias, known as D'Agostini bias [67].

C. Iterative Monte Carlo fitting

In standard single-fit PDF analyses, one often finds that some of the shape parameters in Eq. (35) are not well determined by data and need to be fixed by hand, even when data sets beyond inclusive DIS are considered [21]. This can introduce additional arbitrariness into the analysis, since some of the parameters and distributions have strong correlations. Also, since the χ^2 function is highly nonlinear in the fit parameters, any single fit can find itself trapped in one of many local minima, which only a Monte Carlo sampling can reveal.

For these reasons we have chosen instead to embark on a new approach to global PDF analysis, based on an iterative Monte Carlo fitting method that utilizes data resampling techniques and cross-validation. Data resampling is used as a statistical error analysis method for the extracted distributions as an alternative to the standard error analysis using the Hessian method. Cross-validation is a technique that prevents overfitting, and is necessary in particular when using a large number of fitting parameters. The iterative procedure is summarized in Fig. 1, and involves the following key steps:

1. **Generation of pseudodata sets**:

   Each pseudodata point is drawn from Gaussian sampling using the mean and the uncertainties from the original experimental data values, and is constructed as

   $$\widetilde{\mathcal{D}}_i = \mathcal{D}_i + R_i\,\alpha_i, \tag{43}$$

   where $\mathcal{D}_i$ is an actual experimental data point, α_i is the quadrature sum of the uncorrelated uncertainties, and R_i is a random number distributed from the normal

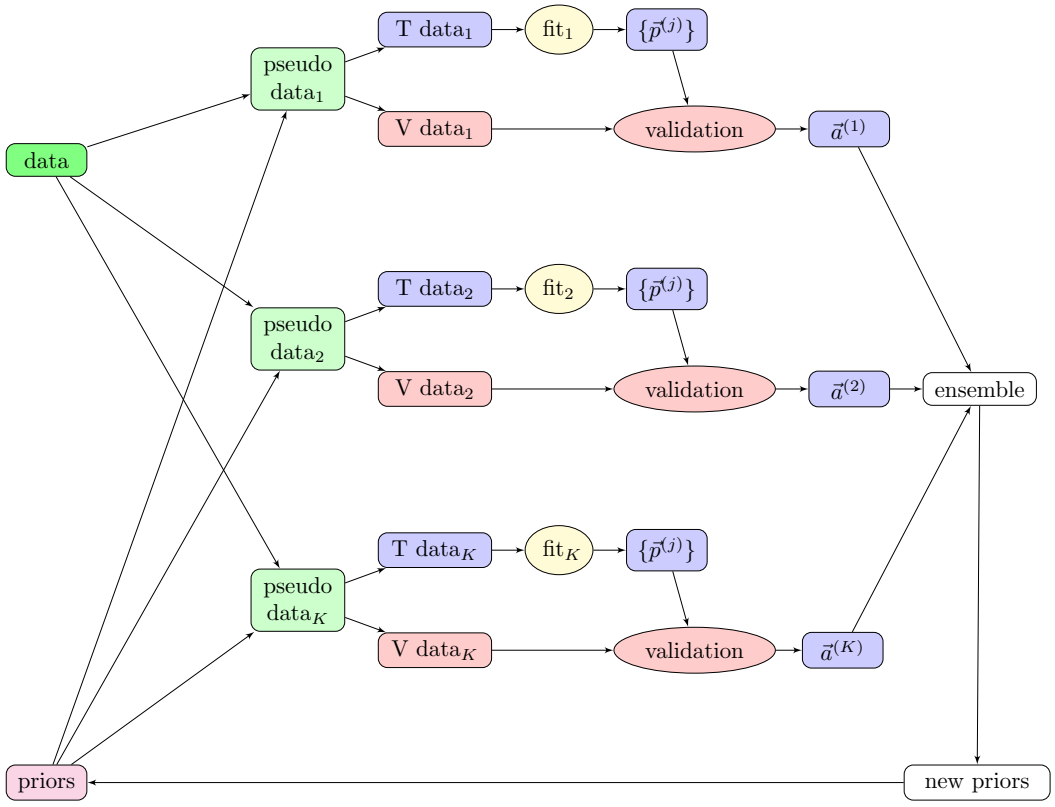

FIG. 1: Schematic illustration of the workflow for the iterative Monte Carlo fitting method. In the first stage, K pseudodata sets are generated, each of which is partitioned into training (T) and validation (V) subsets. For each pseudodata set, the training set is fitted and the parameters $\{\vec{p}^{(j)}\}$ across all the minimization stages j are stored. The cross-validation procedure selects a single set of best fit parameters $\vec{a}^{(l)}$ from $\{\vec{p}^{(j)}\}$ for each pseudodata set l, and the collection of $\{\vec{a}^{(l)}; l = 1, \ldots, K\}$ is then used as the priors for the next iteration.

distribution. A total of K pseudodata sets are generated this way.

2. **Partition of pseudodata sets**:

   Each pseudodata set is partitioned randomly into "training" and "validation" sets using a splitting fraction of 50%/50%. The partition of the data is performed within each experimental data set to avoid experiments with few data points not appearing in many of the fits. Data sets with fewer than 10 points are not partitioned, and are included as part of the training set.

3. **Generation of the priors**:

   The priors are the set of parameters to be used as the starting points for the fits.

During the initial iteration the priors for each fit are generated using flat sampling of the parameter space within a sufficiently broad region. The ensemble of fitted parameters or "posteriors" $\vec{a}^{(l)}$, with $l = 1, \ldots, K$, is then used as the priors for the next iteration.

4. χ^2 **minimization and cross-validation**:
   The Levemberg-Marquardt gradient search algorithm `lmdiff` [68] is used to minimize the χ^2 function of the training data set. Information on the parameters $\{\vec{p}^{(j)}\}$ and the χ^2 values of the training and validation sets across each minimization stage j is recorded. The best fit parameters are selected from the stage in which the lowest value in the validation χ^2 is attained.

As mentioned earlier, the essential idea behind the iterative method is to systematically transform the priors from the initial flat sampling into posteriors that are distributed consistently with the information contained within the data. To assess the convergence of the posterior distributions we examine the convergence of the corresponding $\chi^2_{\rm dof}$ distribution. In practice, the rate of convergence is rather slow if one uses the full set of posteriors from one iteration to the next. To increase the efficiency of the iterative procedure, in practice we select a subset of the posteriors that give the smallest $\chi^2_{\rm dof}$ values, making a cut at the peak in the $\chi^2_{\rm dof}$ distribution in a given iteration. The signature of the convergence is then the presence of an irreducible width in the $\chi^2_{\rm dof}$ distribution that is generated from the selected sample of priors.

In Fig. 2 the mean and the two-sided standard deviation of the training and validation $\chi^2_{\rm dof}$ distributions are shown across the various iterations of the IMC procedure. We find that statistical convergence of the $\chi^2_{\rm dof}$ distribution is achieved after 5 or 6 iterations. Notice that the $\chi^2_{\rm dof}$ distribution peaks around $\chi^2_{\rm dof} \approx 2$, which is the expected behavior in the idealized Gaussian statistics. Namely, the χ^2 values obtained after fitting the many different realizations of the data sets from the resampling are distributed according to the noncentral χ^2 distribution

$$\mathcal{P}(\chi^2; n, \lambda) = \frac{1}{2} \exp\left[-\frac{1}{2}(\chi^2 + \lambda)\right] \left(\frac{\chi^2}{\lambda}\right)^{(n-2)/4} I_{n/2-1}(\sqrt{\lambda\chi^2}), \tag{44}$$

where $I_{n/2-1}$ is the modified Bessel function of the first kind, and n is the number of degrees of freedom ($\approx$ number of data points). The parameter λ is given by a sum of the expectation

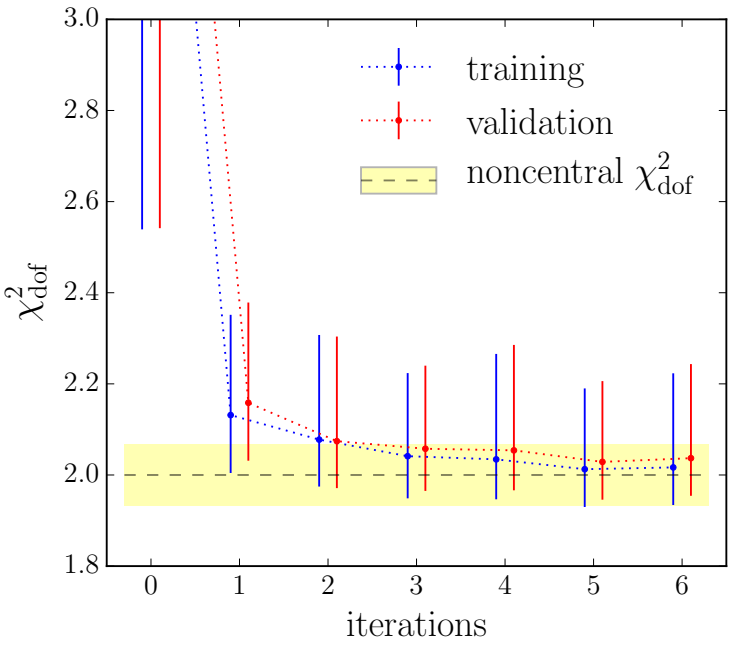

FIG. 2: Mean and two-sided standard deviations of the $\chi^2_{\rm dof}$ distribution as a function of the iteration number for the training (blue points) and validation (red points) data sets, compared with the mean (dashed horizontal line at $\chi^2_{\rm dof} = 2$) and standard deviation (yellow band) for the ideal noncentral $\chi^2_{\rm dof}$ distribution.

values E of the individual point-by-point χ^2_i for the data points, $\lambda = \sum_i^n \mathrm{E}[\chi^2_i]$. In the ideal Gaussian statistics the expectation values are $\mathrm{E}[\chi^2_i] \simeq 1$, and therefore $\lambda \simeq n$. The noncentral χ^2 distribution peaks around $2n$, and the corresponding noncentral $\chi^2_{\rm dof}$ peaks around 2.

For comparison we also include in Fig. 2 the mean and standard deviation for the ideal noncentral $\chi^2_{\rm dof}$ distribution. While the mean values of the IMC and ideal noncentral $\chi^2_{\rm dof}$ distributions are in agreement, the right-side standard deviation is generally larger for the IMC case. This is somewhat consistent with the situation in the standard error analysis in single fits, in which a tolerance in terms of $\Delta\chi^2$ is defined in order to obtain conservative error bands for the extracted PDFs. We stress that in our approach the $\chi^2_{\rm dof}$ distribution is extracted uniquely by the iterative procedure, and is determined purely by the information contained in the data, thus removing the need of any tolerance criterion.

The cross-validation in our procedure is implemented in two steps. The first step is integrated within the iterative procedure and corresponds to the selection of parameters

from the minimization steps, as described above. The logic is that over-fitting is signaled whenever the χ^2 of the training set continues to improve across the minimization steps at the expense of a deteriorating validation χ^2. The second step is implemented once the statistical convergence of the posterior distribution is attained. We then examine each of the final posteriors $\vec{a}^{(l)}$ by checking the difference in the χ^2 values between the validation and training sets. A large difference also signals over-fitting, which can occur if the training set is not a statistically representative sample of the entire data set, resulting in the partition creating an artificial incompatibility within the data set itself. The samples that are ultimately selected are those that satisfy the condition

$$\left|\chi^{2\,(\text{training})}_{\text{dof}} - \chi^{2\,(\text{validation})}_{\text{dof}}\right| < 2\,\epsilon, \tag{45}$$

where ϵ is chosen to be the standard deviation of the ideal noncentral χ^2_{dof} distribution with the number of degrees of freedom equal to the number of points in the training data set.

The final ensemble of posteriors is a collection of points in the parameter space, each of which is represented by the vector $\vec{a}^{(l)}$, whose components are the fitting parameters. The distribution of the parameters is governed by the likelihood function

$$\mathcal{P}(\vec{a}|\mathcal{D}) \propto \exp\left[-\frac{1}{2}\chi^2(\vec{a})\right], \tag{46}$$

where χ^2 is defined as in Eq. (41), and $\mathcal{D}$ denotes the experimental data. The ensemble of posteriors is therefore an approximate Monte Carlo representation of the likelihood function $\mathcal{P}(\vec{a}|\mathcal{D})$ for the fitting parameters $\vec{a}$. The expectation values for the observables, such as a PDF at a given x and Q^2, can then be computed as

$$\mathrm{E}[\mathcal{O}] = \int d\vec{a}\ \mathcal{P}(\vec{a}|\mathcal{D})\ \mathcal{O}(\vec{a}) = \frac{1}{K}\sum_l \mathcal{O}(\vec{a}^{(l)}). \tag{47}$$

In the last equality a Monte Carlo integration is performed by sampling the parameters according to $\mathcal{P}(\vec{a}|\mathcal{D})$, utilizing precisely the samples $\{\vec{a}^{(l)}; l = 1, \ldots, K\}$ obtained after the IMC procedure. Similarly, the variance of the observable can be computed as

$$\mathrm{V}[\mathcal{O}] = \frac{1}{K}\sum_l \left(\mathcal{O}(\vec{a}^{(l)}) - \mathrm{E}[\mathcal{O}]\right)^2, \tag{48}$$

which gives the 1σ confidence interval for the observable $\mathcal{O}$.

Finally, in order to assess the goodness-of-fit, we also compute the standard Pearson's χ^2, defined as

$$\chi^2 = \sum_e \left[\sum_i \left(\frac{\mathcal{D}_i^{(e)} - \mathrm{E}[T_i^{(e)}/N_i^{(e)}]}{\alpha_i^{(e)}} \right)^2 \right], \tag{49}$$

which differs slightly from the definition given in Eq. (41). In particular, the actual data points $\mathcal{D}_i^{(e)}$ are used here instead of the pseudodata points, and the theory values are computed as expectation values in Eq. (47). This definition allows a direct comparison with χ^2 values from single-fit based analyses.

IV. DATA SETS

The JAM15 global PDF analysis uses all available world data on inclusive DIS of leptons (electrons, positrons and muons) on proton, deuteron and ^{3}He targets that pass the required cuts on the invariant final state mass, $W^2 \geq 4$ GeV^2, and $Q^2 \geq 1$ GeV^2 (see Sec. V A). This includes all of the sets from the EMC [69], SMC [70, 71], COMPASS [72, 73], SLAC [74–81], HERMES [82–84], and Jefferson Lab Hall A [85] experiments used in the previous JAM13 global fit [20], as well as the more recent high-precision asymmetry measurements from Jefferson Lab [14–18] and new results from COMPASS [39]. The data sets are summarized in Table I, and the kinematic coverage in x and Q^2 is illustrated in Fig. 3. The Jefferson Lab data points are concentrated at intermediate values of x and $Q^2 \lesssim 5$ GeV^2, and are entirely excluded by a $W^2 \geq 10$ GeV^2 cut, as is typically used in other PDF fits. With the inclusion of the new Jefferson Lab results, the number of data points more than doubles, from ≈ 1000, considered in the JAM13 fit, to > 2500 in the current analysis.

A summary describing most of the earlier experiments from SLAC, CERN, DESY and Jefferson Lab can be found in Ref. [86]; here we give a few experimental details about the most recent experiments from Jefferson Lab [14–18] and COMPASS [39]. All of these experiments can be considered continuations of the extensive experimental programs of the Hall A and CLAS collaborations at Jefferson Lab and COMPASS at CERN.

- **eg1b** Experiment eg1b was the second installment of the eg1 run group in Jefferson Lab's Hall B and ran in 2000–2001. It used the CLAS spectrometer and proton ($^{15}NH_3$) and deuteron ($^{15}ND_3$) targets polarized along the direction of the incoming

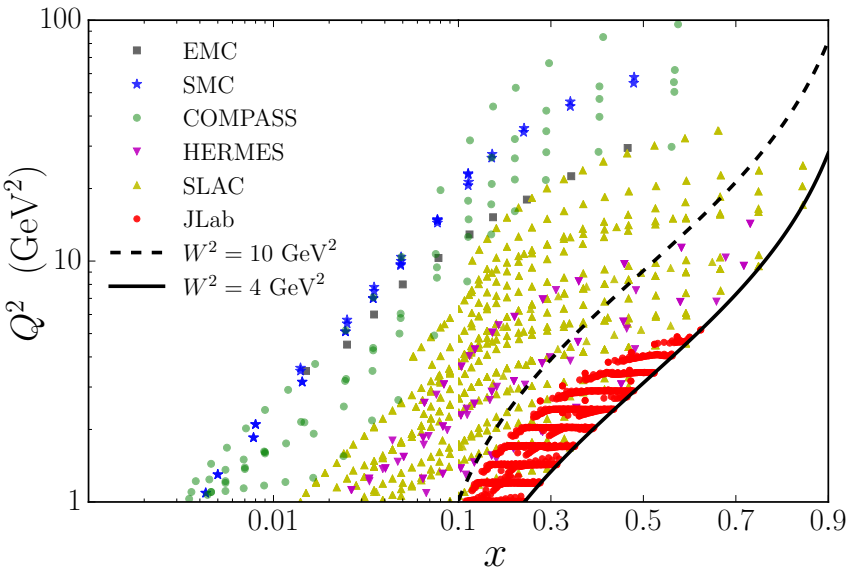

FIG. 3: Kinematic coverage in x and Q^2 of the polarized inclusive DIS data sets used in the JAM15 analysis. The boundaries corresponding to fixed $W^2 = M^2 + Q^2(1-x)/x$ equal to 4 GeV^2 (solid curve) and 10 GeV^2 (dashed curve) are indicated.

electron beam to measure the double spin asymmetry $A_{\parallel}$ in Eq. (3). A first round of publications [12, 13] from this experiment focused on the results from the lowest (1.6 GeV) and highest (5.8 GeV) beam energies. In the meantime, the complete data set (including data with 2.5 and 4.2 GeV beam energy) has been analyzed, including numerous improvements in the procedures used to correct for backgrounds, beam and target polarization, electromagnetic radiative corrections, and kinematic reconstruction. The final results from eg1b for the deuteron have been published [16] and the results for the proton (used in the present analysis) will be published shortly [14]. Due to the wide range in beam energies and running conditions, eg1b covers the largest range in x and Q^2 of any experiment at Jefferson Lab.

- **eg1-dvcs** As the last spin structure function measurement with CLAS in the 6 GeV era of Jefferson Lab, experiment eg1-dvcs ran in 2009 with a significantly improved polarized target ($^{14}NH_3$ and $^{14}ND_3$ polarized along the beam direction) at the highest beam energy ($5.8 - 6$ GeV) available at the time. This experiment differs from eg1b chiefly due to its much higher integrated luminosity and a significantly larger minimum

TABLE I: Inclusive DIS data sets used in the JAM15 global PDF analysis, indicating the observables fitted, the targets used, the number of data points in each experiment, and the respective $\chi^2_{\rm dof}$ values.

experiment	reference	observable	target	# points	$\chi^2_{\rm dof}$
EMC	[69]	A_1	p	10	0.40
SMC	[70]	A_1	p	12	0.47
SMC	[70]	A_1	d	12	1.62
SMC	[71]	A_1	p	8	1.26
SMC	[71]	A_1	d	8	0.57
COMPASS	[72]	A_1	p	15	0.92
COMPASS	[73]	A_1	d	15	0.67
COMPASS	[39]	A_1	p	51	0.76
SLAC E80/E130	[74]	$A_\parallel$	p	22	0.59
SLAC E142	[75]	A_1	^{3}He	8	0.49
SLAC E142	[75]	A_2	^{3}He	8	0.60
SLAC E143	[76]	$A_\parallel$	p	81	0.80
SLAC E143	[76]	$A_\parallel$	d	81	1.12
SLAC E143	[76]	$A_\perp$	p	48	0.89
SLAC E143	[76]	$A_\perp$	d	48	0.91
SLAC E154	[77]	$A_\parallel$	^{3}He	18	0.51
SLAC E154	[77]	$A_\perp$	^{3}He	18	0.97
SLAC E155	[78]	$A_\parallel$	p	71	1.20
SLAC E155	[79]	$A_\parallel$	d	71	1.05
SLAC E155	[80]	$A_\perp$	p	65	0.99
SLAC E155	[80]	$A_\perp$	d	65	1.52
SLAC E155x	[81]	$\widetilde{A}_\perp$	p	116	1.27
SLAC E155x	[81]	$\widetilde{A}_\perp$	d	115	0.83
HERMES	[82]	A_1	"n"	9	0.25
HERMES	[83]	$A_\parallel$	p	35	0.47
HERMES	[83]	$A_\parallel$	d	35	0.94
HERMES	[84]	A_2	p	19	0.93
JLab E99-117	[85]	$A_\parallel$	^{3}He	3	0.27
JLab E99-117	[85]	$A_\perp$	^{3}He	3	1.58
JLab E06-014	[17]	$A_\parallel$	^{3}He	14	2.12
JLab E06-014	[18]	$A_\perp$	^{3}He	14	1.06
JLab eg1-dvcs	[15]	$A_\parallel$	p	195	1.52
JLab eg1-dvcs	[15]	$A_\parallel$	d	114	0.94
JLab eg1b	[14]	$A_\parallel$	p	890	1.11
JLab eg1b	[16]	$A_\parallel$	d	218	1.02
total				2515	1.07

scattering angle, yielding a much higher statistical precision in the DIS region. Its results have been published in Ref. [15].

- **E06-014** Experiment E06-014 ran in Hall A of Jefferson Lab in 2009 with the primary purpose of determining the higher twist moment $d_2(Q^2)$ in Eq. (23) for the neutron. It measured both parallel and transverse double spin asymmetries as in Eqs. (3) and (4), as well as cross section differences for electron scattering off ^{3}He targets polarized up to 50% through spin-exchange optical pumping. The use of two beam energies (4.7 and 5.9 GeV) and the "BigBite" large acceptance spectrometer resulted in a broad coverage of the DIS region for both d_2 [18] and A_1 [17].

- **COMPASS** The final results of the 2011 run of the COMPASS experiment with a 200 GeV muon beam and a longitudinally polarized proton (NH_3) target have recently been published [39]. Only the virtual photon asymmetry A_1 is given, but at the high Q^2 of these data, corrections due to A_2 should be minimal. COMPASS data provide the lowest accessible values for x and the largest Q^2 values for any given x, and are therefore very important for the extraction of sea quark and gluon polarization information from inclusive DIS data.

For all experiments where they are available, we fit directly the measured asymmetries $A_\parallel$ [Eq. (3)] and $A_\perp$ [Eq. (4)] rather than derived quantities, such as A_1 and A_2. The SLAC experiment E155x [81] presents a special case, in that the target was not polarized exactly at 90° relative to the beam direction, but at 92.4°. In addition, the asymmetries were measured simultaneously by three spectrometers, one of which was on the opposite side of the beam line than the other two, which affects the definitions of the angles θ^* and ϕ^* in Eq. (1). Consequently, the average values of θ^* and ϕ^* must be calculated for each kinematic bin, and Eq. (1) used to relate the measurement to the underlying physics quantities in the fit. The transverse asymmetry measured in this experiment is therefore indicated by the symbol $\widetilde{A}_\perp$ in Table I to differentiate it from the usual $A_\perp$.

By far the largest number of data points (albeit in a limited kinematic range — see Fig. 3) is provided by the eg1b [14, 16] and eg1-dvcs [15] experiments, which account for nearly half of the total. Due to the high statistical precision of these experiments (especially eg1-dvcs), it is important to treat systematic uncertainties properly in order to avoid unwarranted biases in the fit. As outlined in Sec. III C, we distinguish between uncorrelated systematic

uncertainties, which randomly vary from one kinematic bin to the next, and correlated systematic uncertainties, which change the normalization of all data points from a given experiment by essentially the same factor. The former are added in quadrature to the statistical uncertainties (yielding the total point-to-point uncertainties $\alpha_i^{(e)}$ in Eq. (41)), while the latter are incorporated in the normalization factor $N_i^{(e)}$ as defined in Eq. (42).

For most experiments, the correlated systematic uncertainty is just the uncertainty on an overall normalization constant incorporating the dilution factor and the beam and target polarization; in that case the ratio $\beta_{k,i}^{(e)}/\mathcal{D}_i^{(e)}$ in Eq. (42) is simply a constant percentage which we take from the quoted normalization uncertainty. For the proton and deuteron data from the most recent CLAS experiments [14–16], a somewhat more elaborate procedure is used, since an overall normalization factor uncertainty is not available for these data. In the case of eg1-dvcs [15], the quoted systematic uncertainties for all kinematic bins is completely dominated by correlated normalization uncertainties. Those quoted uncertainties are therefore used directly for the quantity $\beta_{k,i}^{(e)}$ in Eq. (42) (with the proper sign equal to that of the data point in question and, since only one source of correlated systematic error is quoted, $k = 1$), without adding anything to the statistical uncertainties.

For the proton data from eg1b [14], only a small amount of correlation, of order 3% of the magnitude of the measured asymmetry, is found between the systematic uncertainties for different kinematic bins. We therefore assign $\beta_{k=1,i}^{(e)}/\mathcal{D}_i^{(e)} = 0.03$ for all bins, but add the full systematic uncertainty in quadrature to the statistical errors for $\alpha_i^{(e)}$. Finally, for the eg1b deuteron data set [16] one finds a correlated systematic uncertainty of about 14% for the 5.7 GeV data ($\beta_{1,i}^{(e)}/\mathcal{D}_i^{(e)} = 0.14$) and 7% for the 4.2 GeV data ($\beta_{1,i}^{(e)}/\mathcal{D}_i^{(e)} = 0.07$). Since this correlated part of the overall uncertainty is quite sizable, it is subtracted from the quoted systematic uncertainties in each bin. The uncorrelated uncertainty $\sigma_{\rm uncor} = \sqrt{\sigma_{\rm tot\ sys}^2 - (\beta_{1,i}^{(e)})^2}$ is then added in quadrature to the statistical uncertainties. In all cases the factors $r_k^{(e)}$ are optimized in the fit, and the results indicate by which fraction of the correlated uncertainties the data points of a given experiment have to be moved to best agree with the world data.

V. RESULTS

In this section we present the main results of the JAM15 global analysis for the spin-dependent twist-2 and twist-3 distributions and moments, and assess in particular the impact of the new Jefferson Lab data on the PDFs and their uncertainties. Before presenting the main results of the fits, we first examine the dependence of the results on the kinematic cuts applied to the data in order to maximize the range of W^2 and Q^2 over which the data can be accommodated within our theoretical framework.

As mentioned above, for the initial iteration the priors for each fit are generated from flat sampling of a reasonable range in the parameter space. While any restriction of the initial parameter sampling in principle introduces a bias into the procedure, we choose the parameter ranges to be sufficiently broad so as to minize any such bias, at the same time ensuring that the parameters do not introduce unphysical behavior in any of the observables.

Specifically, for the exponent a governing the $x \to 0$ behavior of the leading twist PDFs in Eq. (35), we consider the range $a \in [-1, 0]$, which covers the values expected from Regge theory, as well as the findings in all previous phenomenological PDF analyses. For the exponent b that determines the $x \to 1$ behavior, we choose the range $b \in [2, 5]$ for the Δu^+ and Δd^+ PDFs that have valence components at large x, and $b \in [2, 10]$ for the sea distributions Δs^+ and Δg that are more strongly suppressed as $x \to 1$. In addition, we introduce penalties in the χ^2 whenever the b parameter for Δs^+ or Δg becomes lower than the corresponding parameter for Δd^+. For the auxiliary c and d shape parameters in Eq. (35), we set the starting ranges for both between -1 and 1. For the normalization of the singlet quark and gluon first moments, we take the starting values such that $\Delta\Sigma$ and ΔG are both equal to 0.5.

Considerably less is known about the shapes of the higher twist distributions. Generally, these are expected to play a greater role at smaller W values, or, for fixed Q^2, at large x. To allow for additional suppression of the higher twists at small x, we consequently take the initial range for the a parameter for the twist-3 and twist-4 functions to be $a \in [-1, 1]$, with normalization for all higher twists starting at zero. For the large-x parameter b we take the initial sampling region to be $b \in [2, 5]$, and for the auxiliary parameters $c, d \in [-1, 1]$ for all higher twist distributions.

TABLE II: Dependence of the global fits on the cut on the hadronic final state mass squared, $W^2_{\rm cut}$, for a fixed $Q^2_{\rm cut} = 1$ GeV^2. The $\chi^2_{\rm dof}$ values and the number of points included by the different W^2 cuts are listed, with the values for the JAM15 fit indicated in boldface.

$W^2_{\rm cut}$ (GeV^2)	3.5	**4**	5	6	8	10
# points	2868	**2515**	1880	1427	943	854
$\chi^2_{\rm dof}$	1.20	**1.07**	1.03	1.02	0.99	0.97

TABLE III: Dependence of the global fits on the cut on the four-momentum transfer squared, $Q^2_{\rm cut}$, for a fixed $W^2_{\rm cut} = 4$ GeV^2. The $\chi^2_{\rm dof}$ values and number of points included by the different Q^2 cuts are listed, with the JAM15 fit values indicated in boldface.

$Q^2_{\rm cut}$ (GeV^2)	**1.0**	2.0	4.0
# points	**2515**	1421	611
$\chi^2_{\rm dof}$	**1.07**	1.08	0.95

A. W^2 and Q^2 cuts

To determine how far the kinematic boundaries delimited by the W^2 and Q^2 cuts can be extended, we perform a series of IMC fits, varying $W^2_{\rm cut}$ between 3.5 and 10 GeV^2 and $Q^2_{\rm cut}$ between 1 and 4 GeV^2. The results of the fits are summarized in Tables II and III, where the $\chi^2_{\rm dof}$ values are given, along with the number of points included with each combination of cuts. For a fixed $Q^2_{\rm cut} = 1$ GeV^2, the number of points more than triples when going from $W^2_{\rm cut} = 10$ GeV^2 to 3.5 GeV^2, mostly due to the inclusion of the Jefferson Lab data, but also because of important contributions from SLAC data. Clearly, for the larger $W^2_{\rm cut}$ values very good fits can be obtained with $\chi^2_{\rm dof} \approx 1$, which increases very gradually as more data allowed by lower W^2 cuts are included in the fits. For the lowest W^2 cut of 3.5 GeV^2, there is a somewhat larger increase in the $\chi^2_{\rm dof}$ value.

On the other hand, it is known that χ^2 alone is not always a sufficient indicator of the quality of the fit. To examine the cut dependence in more detail, in Fig. 4 we show

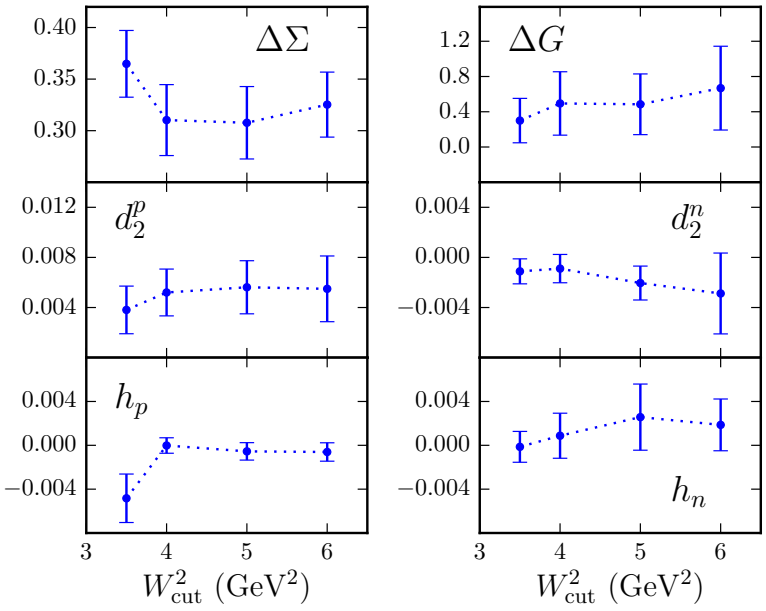

FIG. 4: Dependence on $W^2_{\rm cut}$ of several moments of twist-2 PDFs ($\Delta\Sigma$ and ΔG), the twist-3 d_2 moments, and the third moments h_p and h_n of the twist-4 distributions of the proton and neutron. All fits use $Q^2_{\rm cut} = 1$ GeV^2, and the moments are truncated moments evaluated in the measured region between $x = 0.001$ and 0.8.

several moments of PDFs for $W^2_{\rm cut}$ between 3.5 and 6 GeV^2, where the greatest variations are expected to occur. For higher values of $W^2_{\rm cut}$, the results between 6 and 10 GeV^2 do not change appreciably. To avoid extrapolations into unmeasured regions of x, we compute here the truncated moments, evaluated between $x = 0.001$ and 0.8, in the region covered by the inclusive DIS data sets. The lowest moment of the twist-2 quark singlet distribution $\Delta\Sigma$ is found to be rather stable down to $W^2_{\rm cut} = 4$ GeV^2, increasing by $\sim 1\sigma$ at $W^2_{\rm cut} = 3.5$ GeV^2. Similarly, the lowest moment of the gluon distribution ΔG is relatively flat as a function of $W^2_{\rm cut}$.

For the twist-3 d_2 proton and neutron moments, the variation across $W^2_{\rm cut}$ is also fairly weak, although a significant reduction in the uncertainty on the neutron d_2^n is observed when more of the low-W^2 data are included. The impact of the low-W^2 data is even more dramatically illustrated for the case of the third moment of the twist-4 distribution of the proton H_p, which shows a clear change in its central value between $W^2_{\rm cut} = 3.5$ and 4 GeV^2, and a significantly larger uncertainty at the lower cut. A stronger impact of low-W^2 data on

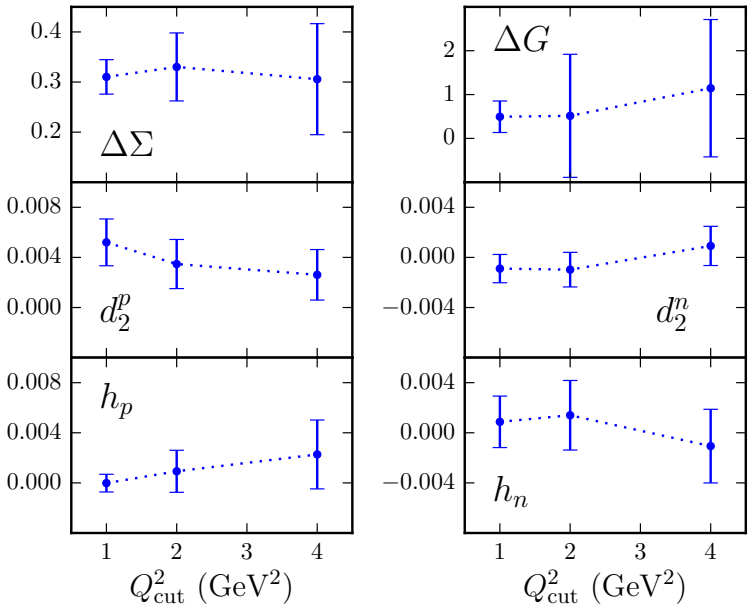

FIG. 5: As in Fig. 4, but for varying values of $Q^2_{\rm cut}$ between 1 and 4 GeV^2, for a fixed $W^2_{\rm cut} = 4$ GeV^2.

higher twist contributions is not surprising, given that higher twists are expected to be more important at larger x values, and the more rapid variation may be a signal of the presence of yet higher twist corrections from the nucleon resonance region beyond those considered in our analysis (see Sec. II B).

The dependence of the moments on the Q^2 cut is shown in Fig. 5. The variation between $Q^2_{\rm cut} = 1$ and 4 GeV^2 is generally mild and consistent within the errors. Because of the reduced statistics for increasing values of $Q^2_{\rm cut}$ (from $\sim$ 2500 data points at 1 GeV^2 to $\sim$ 1400 points at 2 GeV^2, and $\sim$ 600 at 4 GeV^2), the uncertainties on the moments are correspondingly larger. For the leading twist $\Delta\Sigma$ and ΔG moments, for example, the uncertainties increase 3–4 fold between $Q^2_{\rm cut} = 1$ and 4 GeV^2. With the aim of utilizing the maximum number of data points possible across all W^2 and Q^2 regions, while maintaining stable fits with good χ^2 values, we therefore select $W^2_{\rm cut} = 4$ GeV^2 and $Q^2_{\rm cut} = 1$ GeV^2 for the cuts to be used in the final JAM15 analysis. All the results in the following sections will be based on these values.

B. Comparisons with experimental asymmetries

The $\chi^2_{\rm dof}$ values for the individual data sets fitted in the JAM15 analysis are listed in Table I. The overall $\chi^2_{\rm dof}$ is 1.07 for the 2515 data points in the global data set. The fits to the complete set of asymmetries used in analysis are illustrated in Figs. 6–14. In particular, the proton longitudinal polarization asymmetries $A_\parallel^p$ and A_1^p from the EMC [69], SMC [70, 71], COMPASS [39, 72], SLAC [74, 76, 78] and HERMES [83] experiments are shown in Fig. 6 as a function of x, for the various Q^2 ranges measured in the experiments, ranging from $Q^2 = 1$ GeV^2 to ~ 100 GeV^2. In each panel the measured asymmetries are compared with the central values and uncertainties for the JAM15 fits, along with the contributions to the asymmetries from leading twist only (which include TMCs but not the higher twist terms). The agreement between the JAM15 fit and the data is generally very good over the entire range of x and Q^2 spanned by these data, and, with the exception of the most recent SMC [71] and SLAC E155 [78] data, the $\chi^2_{\rm dof}$ values for each experiment are less than one.

The error bars on each of the data points represent uncorrelated uncertainties, while the upward or downward shifts of the data points due to their correlated uncertainties are indicated by the upper (green) and lower (blue) bands, denoted by "syst(+)" and "syst(−)", respectively. As discussed in Sec. III B, these shifts are computed by fitting the point-by-point normalization factors $N_i^{(e)}$ in Eq. (42) for each experimental data set. The central values of the data points shown in Figs. 6–14 are then computed as

$$\widetilde{\mathcal{D}}_i^{(e)} = N_i^{(e)} \mathcal{D}_i^{(e)}, \tag{50}$$

and the uncorrelated uncertainties are given by

$$\widetilde{\alpha}_i^{(e)} = N_i^{(e)} \alpha_i^{(e)}. \tag{51}$$

The systematic shifts syst($\pm$) are computed as the difference $\widetilde{\mathcal{D}}_i^{(e)} - \mathcal{D}_i^{(e)}$ of the data points from their nominal values.

The data on the proton transverse polarization asymmetries $A_\perp^p$ and A_2^p from the SLAC [76, 80, 81] and HERMES [84] experiments are compared in Fig. 7 with the JAM15 results. The transverse asymmetries are generally very small, which requires high precision experiments to extract nonzero values. The agreement between the fit and the data is very good overall, with $\chi^2_{\rm dof} \sim 1$ for all experiments other than SLAC E155x [81], where

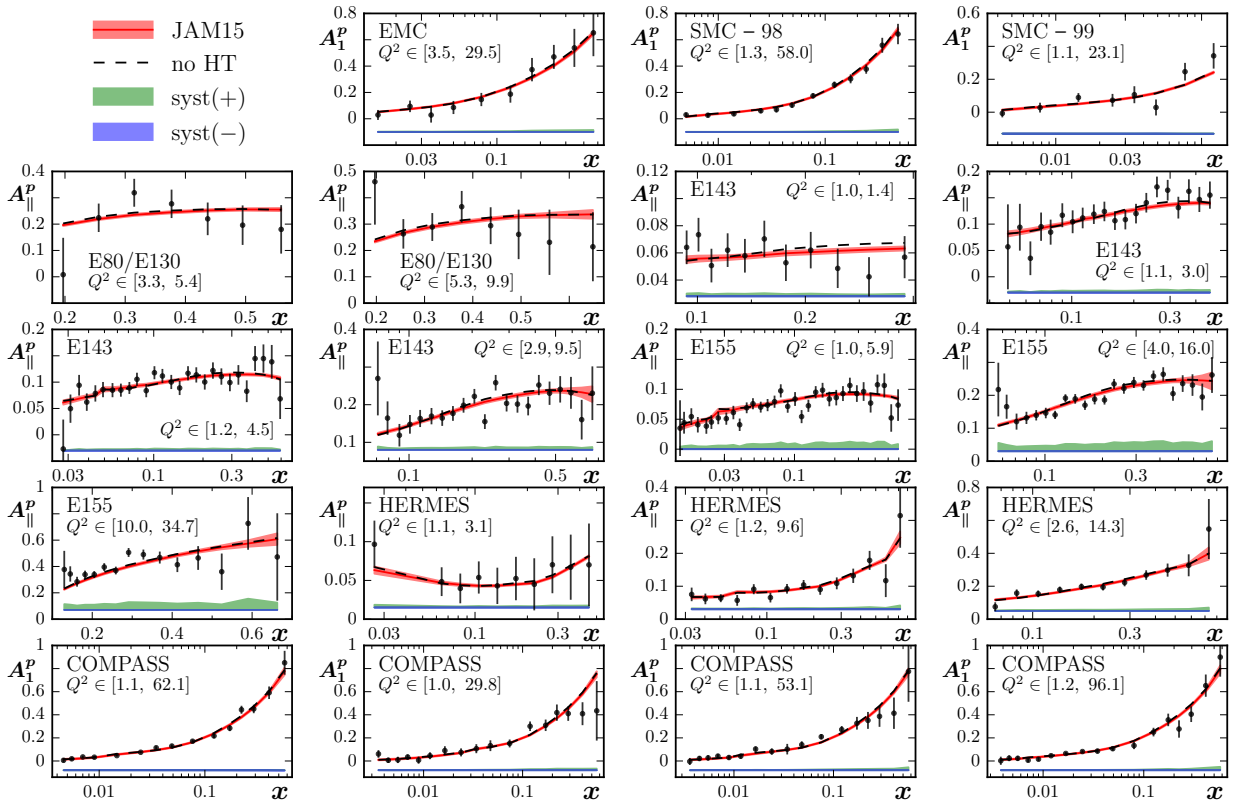

FIG. 6: Proton longitudinal polarization asymmetries $A_\parallel^p$ and A_1^p from EMC [69], SMC [70, 71], COMPASS [39, 72], SLAC [74, 76, 78] and HERMES [83] experiments. The Q^2 range (in units of GeV^2) for the data in each panel is indicated. The data are compared with the asymmetries from the JAM15 fit (solid red curves with bands indicating 1σ uncertainties) and the contributions excluding higher twists (HT) (black dashed curves). The experimental data points include the normalization factors, and the systematic error bands indicate the positive (upper green ["syst(+)"] bands) or negative (lower blue ["syst(−)"] bands) shifts of the data from their nominal values. Panels without visible systematic shifts correspond to data sets for which correlated uncertainties were not provided.

$\chi^2_{\rm dof} = 1.27$. For both the longitudinal and transverse asymmetries, the differences between the full JAM15 fit results and the leading twist contributions are very small. There is an indication of a slightly negative higher twist contribution in the $A_\parallel^p$ data at $x \approx 0.2 - 0.4$ for $Q^2 \lesssim 1.5$ GeV^2 in the SLAC E155 data [78], and a slightly positive higher twist in the $A_\perp^p$ data at larger x values.

The effects of higher twists are more evident in the new Jefferson Lab data in Figs. 8

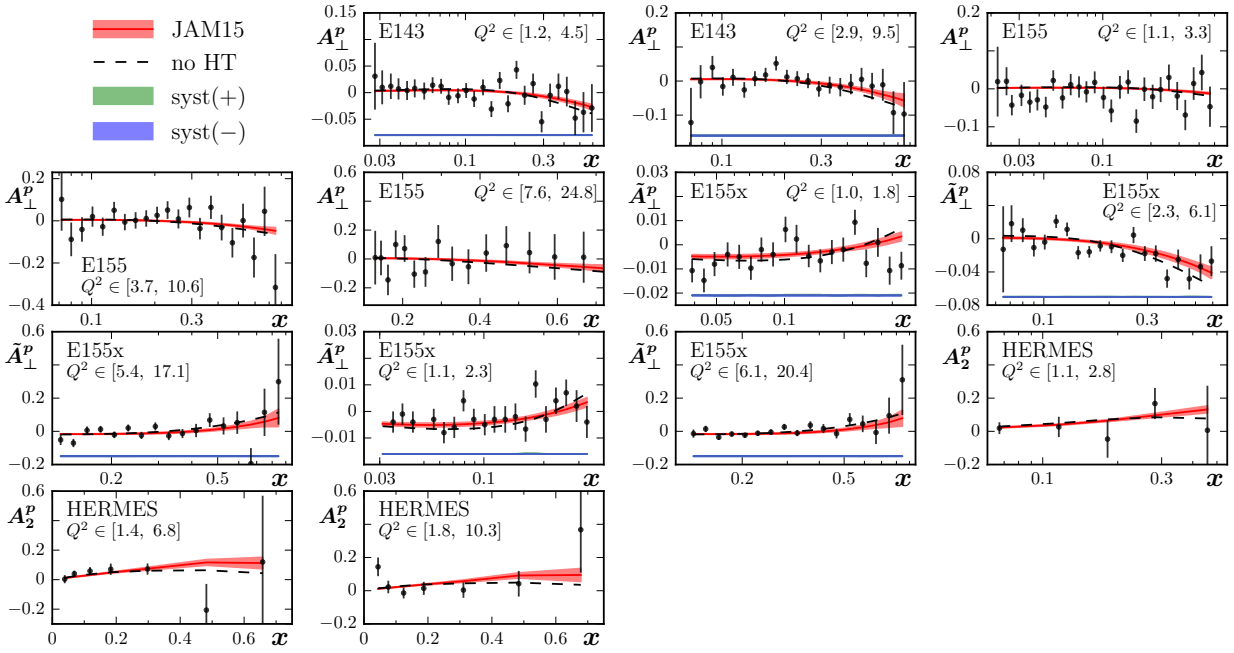

FIG. 7: Proton transverse polarization asymmetries $A_\perp^p$ and A_2^p from SLAC [76, 80, 81] and HERMES [84]. The curves and legends are as in Fig. 6.

and 9, where the longitudinal proton asymmetries $A_\parallel^p$ from the CLAS eg1-dvcs [15] and eg1b [14] experiments, respectively, are compared with the JAM15 fit. (No Jefferson Lab transverse polarization data currently exist for the proton, but will be available soon from the SANE experiment in Hall C [87].) The higher twists are generally negative and lead to a decrease in $A_\parallel^p$ at the larger x values ($x \gtrsim 0.2$) and low $Q^2 \lesssim 2$ GeV^2. For the eg1b proton data, the fit to the nearly 900 points, in fine bins of x and Q^2, gives $\chi^2_{\rm dof} = 1.11$, indicating relatively good agreement with both the lower energy $E = 4.2$ GeV and higher energy $E = 5.7$ GeV data. In some of the eg1b spectra (for example, in the $E = 4.2$ GeV, $Q^2 \in [1.3, 1.4]$ GeV^2 panel) there appear to be strong correlations among the data, although these do not significantly affect the overall $\chi^2_{\rm dof}$.

The eg1-dvcs data, on the other hand, have extremely small statistical uncertainties and are more difficult to accommodate within the global fit, as evidenced by the overall $\chi^2_{\rm dof} = 1.52$ for this data set. This suggests that the uncorrelated uncertainties here may be underestimated, particularly for the $E = 6$ GeV data. The very small errors on this data set dominate the χ^2 fit to the Jefferson Lab data, and lead to an upward systematic pull on the eg1b data, as indicated by the predominantly syst(+) band for the correlated uncertainties.

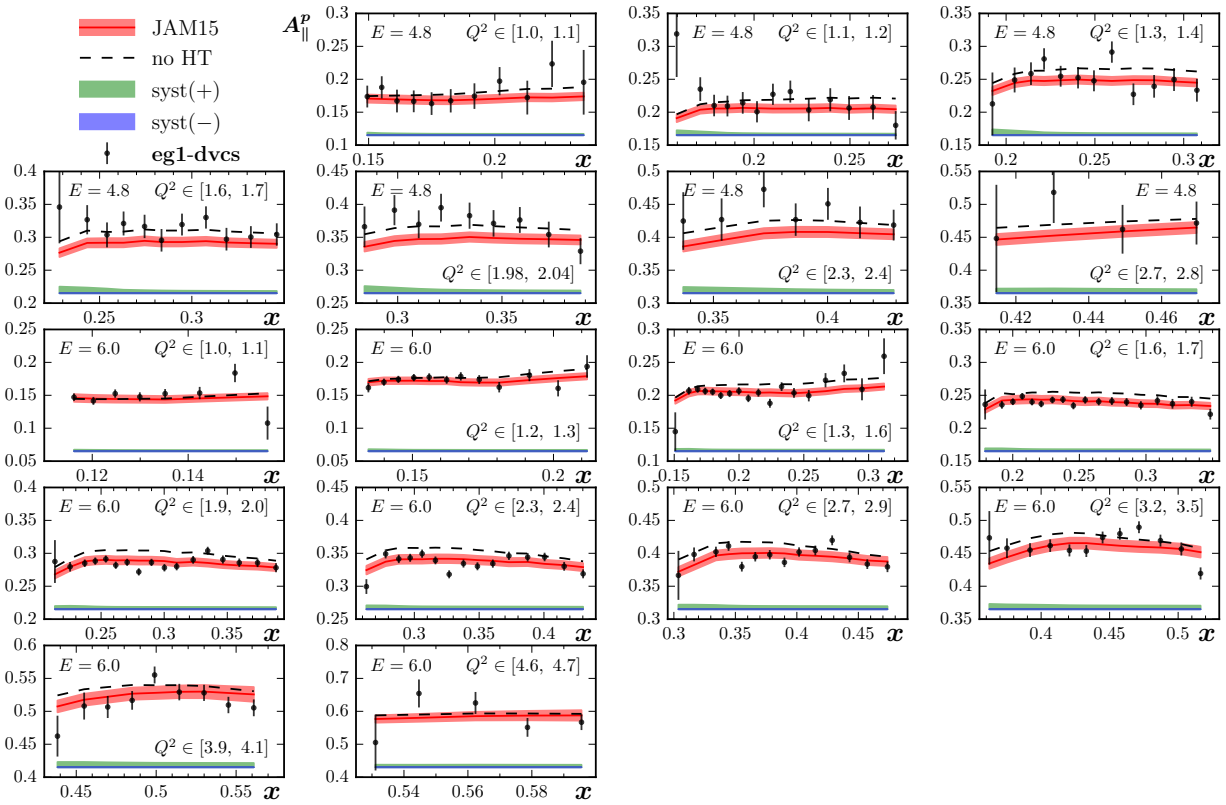

FIG. 8: Proton longitudinal polarization asymmetries $A_\parallel^p$ from the eg1-dvcs [15] experiment at Jefferson Lab. The energies E (in GeV) and Q^2 ranges (in GeV^2) for each panel are indicated. The curves and legends are as in Fig. 6.

A comparison of the entire eg1-dvcs data set reveals the existence of a possible tension between the $E = 4.8$ GeV and 6 GeV data, with the fitted results lying systematically below the lower-energy data for $Q^2 \approx 1.5 - 2.5$ GeV^2. Large systematic shifts of the data relative to the JAM15 fit are less evident for the $E = 6$ GeV data because the smaller uncertainties here provide a stronger pull on the fit.

Similar features are seen in the deuteron longitudinal and transverse asymmetry data, illustrated in Figs. 10 and 11, respectively, for the earlier measurements from SMC [70, 71], COMPASS [72], SLAC [76, 79–81] and HERMES [83]. Generally the deuteron asymmetry data have larger uncertainties compared with the proton data. Most of the data sets can be well described by the global fit, with only the SMC A_1^d data [70] and E155 $A_\perp^d$ data [79] having moderately large $\chi^2_{\rm dof}$ values (1.26 and 1.52, respectively). The former comes mostly from the small errors on the low-x data, while the scatter of the points in the latter, especially at

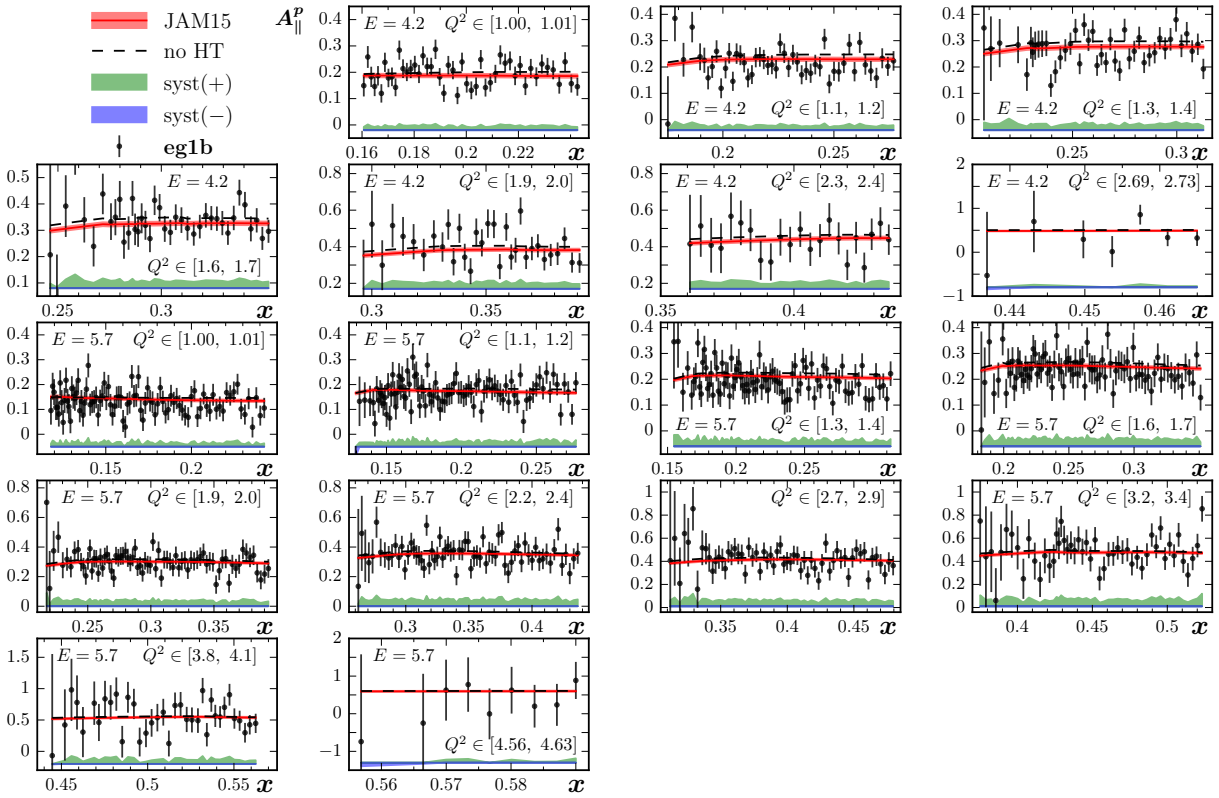

FIG. 9: Proton longitudinal polarization asymmetries $A_\parallel^p$ from the eg1b [14] experiment at Jefferson Lab. The curves and legends are as in Fig. 8.

the higher Q^2 values, suggests a possible underestimation of uncorrelated uncertainties. For the longitudinal asymmetries $A_\parallel^d$ and A_1^d the differences between the full JAM15 results and the leading twist contributions is negligible. For the transverse polarization asymmetries $A_\perp^p$ there is a slight indication of nonzero higher twists at the highest x values, but the effects are very small on the scale of the experimental uncertainties.

The more recent deuteron $A_\parallel^d$ data from the Jefferson Lab eg1-dvcs [15] and eg1b [16] experiments are shown in Figs. 12 and 13, respectively, compared with the JAM15 fit. Good fits with $\chi^2_{\rm dof} \approx 1$ are found for both the eg1-dvcs and eg1b data sets. The similarity between the full results and the leading twist contributions indicates no significant higher twists within the experimental uncertainties. The systematic shifts syst($\pm$) for the deuteron data are much smaller than for the corresponding proton asymmetries, mostly because of the somewhat larger uncorrelated uncertainties. For the eg1b data there is a small tendency for the global fit to overestimate the experimental asymmetries, especially for the $E = 5.7$ GeV

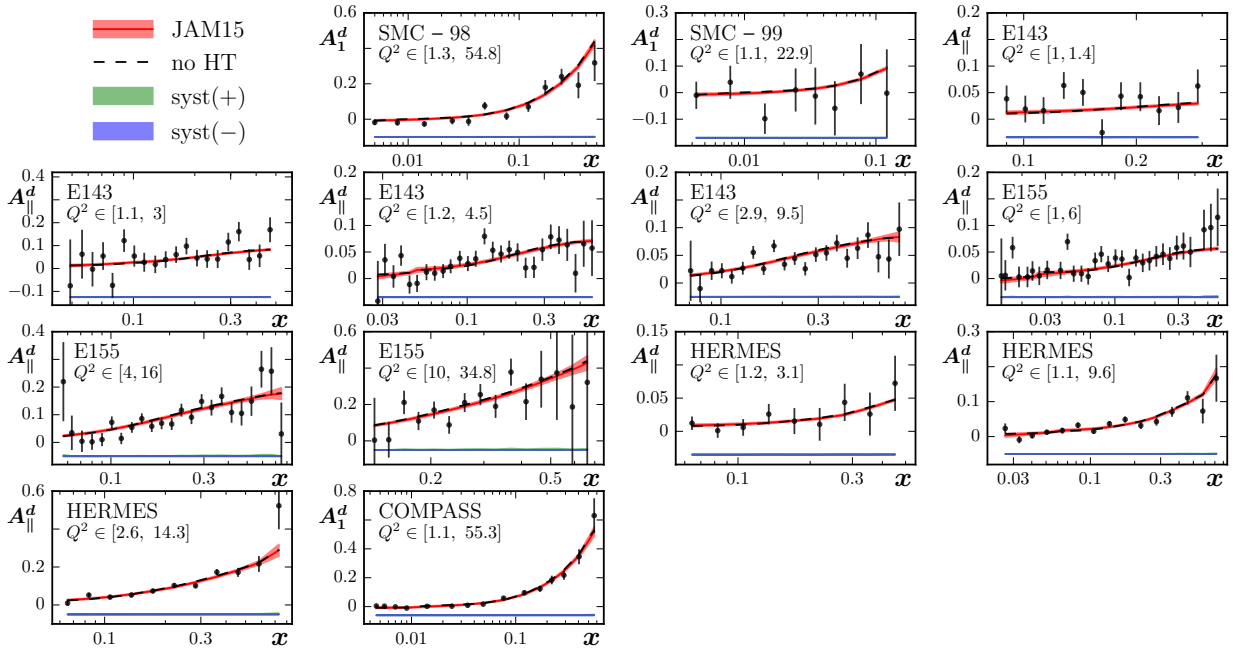

FIG. 10: Deuteron longitudinal polarization asymmetries $A_\parallel^d$ and A_1^d from SMC [70, 71], COMPASS [72], SLAC [76, 79] and HERMES [83] experiments. The curves and legends are as in Fig. 6.

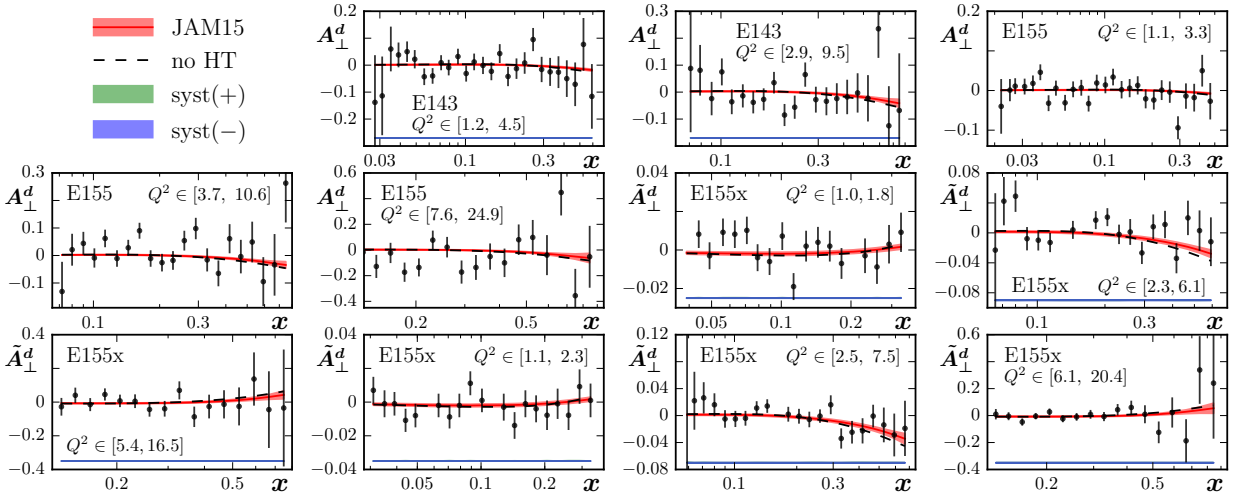

FIG. 11: Deuteron transverse polarization asymmetries $A_\perp^p$ from SLAC [76, 80, 81] data. The curves and legends are as in Fig. 6.

energy data.

Finally, the world's data on longitudinal and transverse polarization asymmetries of ^{3}He are displayed in Fig. 14 for the SLAC E142 [75] and E154 [77] experiments, and the E99-117

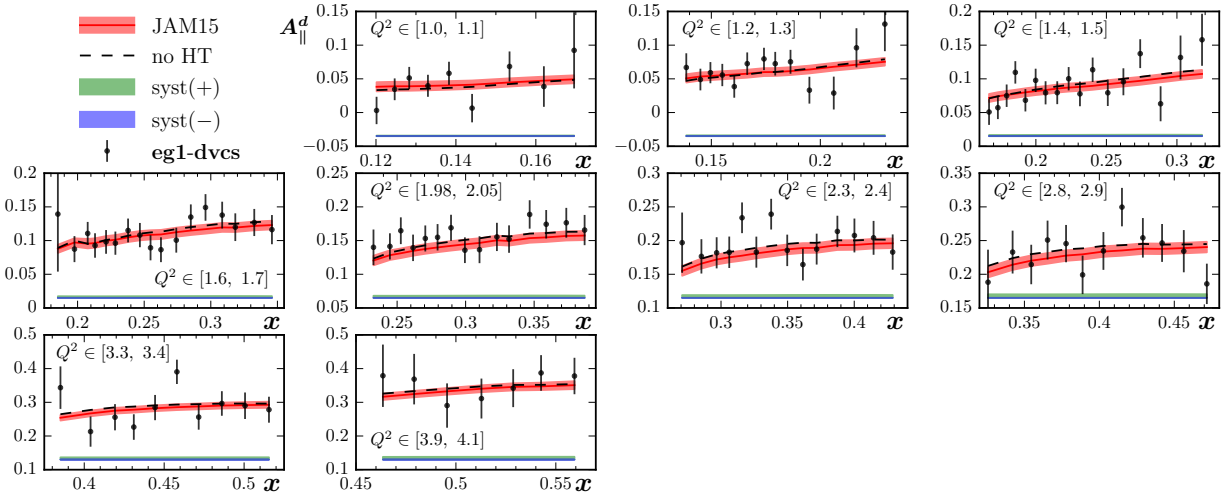

FIG. 12: Deuteron longitudinal polarization asymmetries $A_\parallel^d$ from the eg1-dvcs [15] experiment at Jefferson Lab's Hall B. The curves and legends are as in Fig. 8.

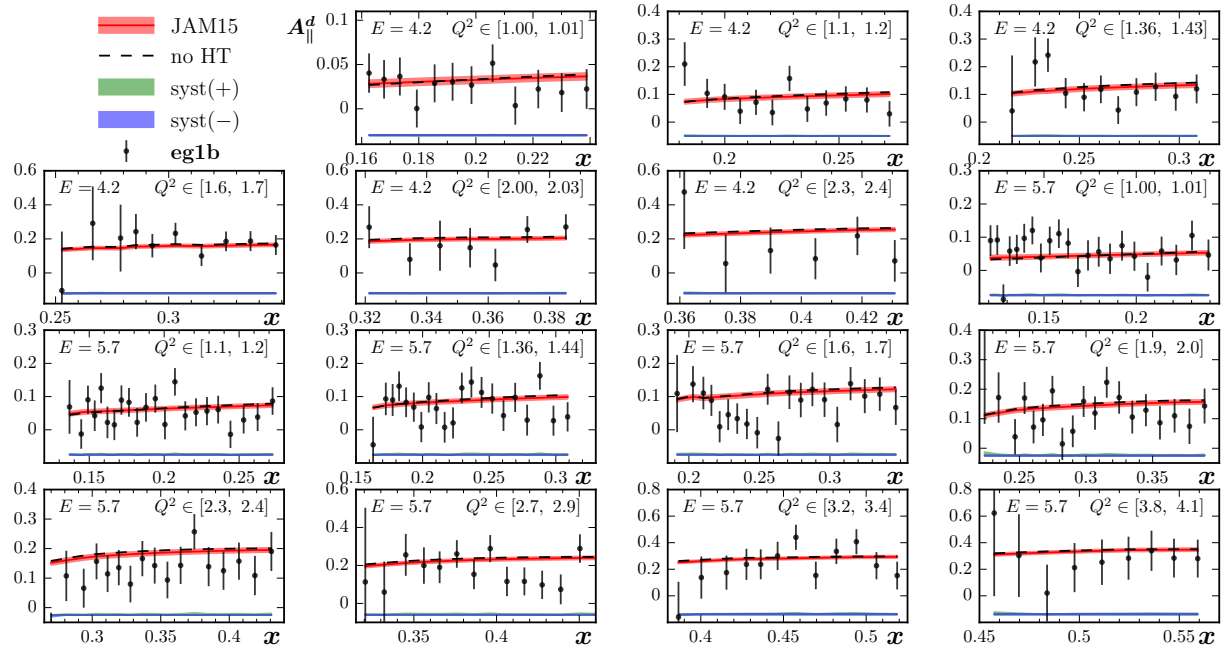

FIG. 13: Deuteron longitudinal polarization asymmetries $A_\parallel^d$ from the eg1b [16] experiment at Jefferson Lab. The curves and legends are as in Fig. 8.

[85] and E06-014 [17, 18] experiments in Jefferson Lab's Hall A. As in the case of the deuteron data, there is no evidence for large higher twists in the $A_\parallel^{\rm He}$ asymmetries, but an indication of a small negative higher twist contribution to $A_\perp^{\rm He}$ in the E06-014 data at the lower Q^2

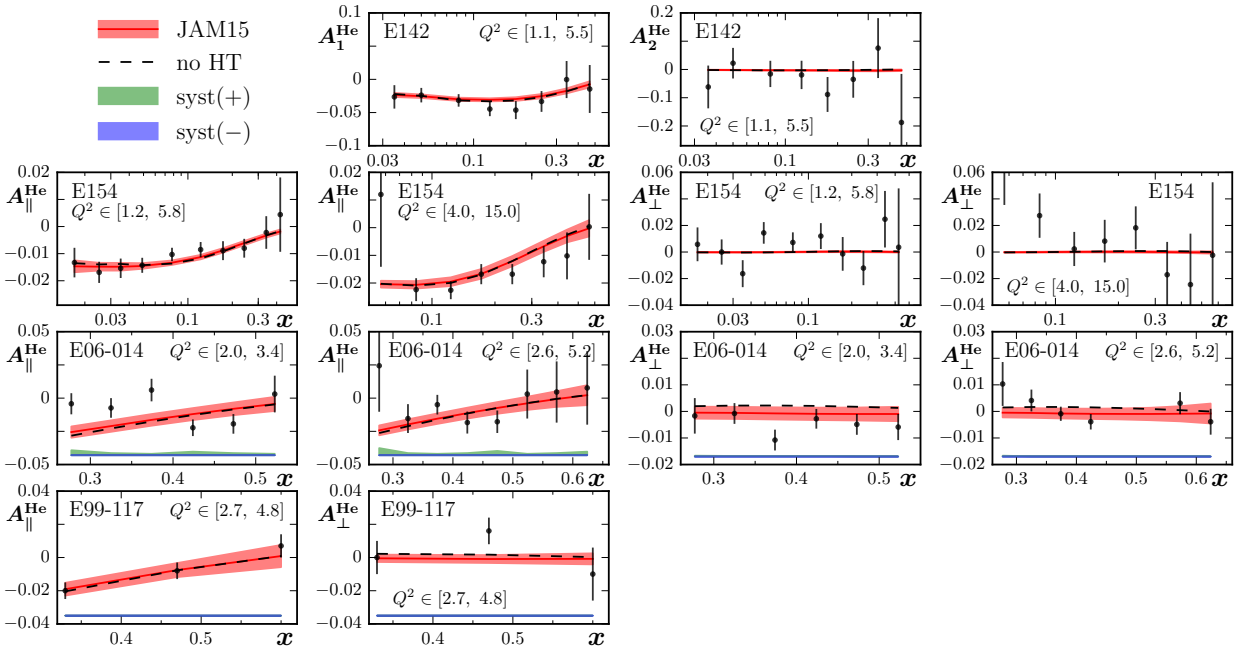

FIG. 14: ^{3}He longitudinal ($A_\parallel^{\rm He}$, $A_1^{\rm He}$) and transverse ($A_\perp^{\rm He}$, $A_2^{\rm He}$) polarization asymmetries from SLAC [75, 77] and Jefferson Lab [17, 18, 85] experiments, compared with the JAM15 global fit. The curves and legends are as in Fig. 6.

values. Generally the fits give small $\chi^2_{\rm dof}$ values for all the longitudinal asymmetry data sets, with the exception of the E06-014 $A_\parallel^{\rm He}$ data set which has $\chi^2_{\rm dof} = 2.12$. Comparison with the JAM15 fit here suggests an incompatibility with the data at the smaller x values. Similarly, good fits are also obtained for the transverse polarization data, with a large $\chi^2_{\rm dof}$ ($\gtrsim 1.5$) observed only for the E99-117 $A_\perp^{\rm He}$ data. However, this comes mostly from a single datum, and because the data set contains a total of only 3 points.

C. Impact of JLab data

To assess more quantitatively the impact of the new Jefferson Lab data on the global fit, we perform an independent IMC analysis of the world's data without inclusion of any of the measurements from Refs. [14–18, 85]. The results of the IMC fits with and without the Jefferson Lab data are presented in Fig. 15 for the twist-2 Δu^+, Δd^+, Δs^+ and Δg PDFs, the twist-3 D_u and D_d PDFs, and the twist-4 proton and neutron distributions H_p and H_n, as a function of x at $Q^2 = 1$ GeV^2. Although the complete IMC analysis contains around

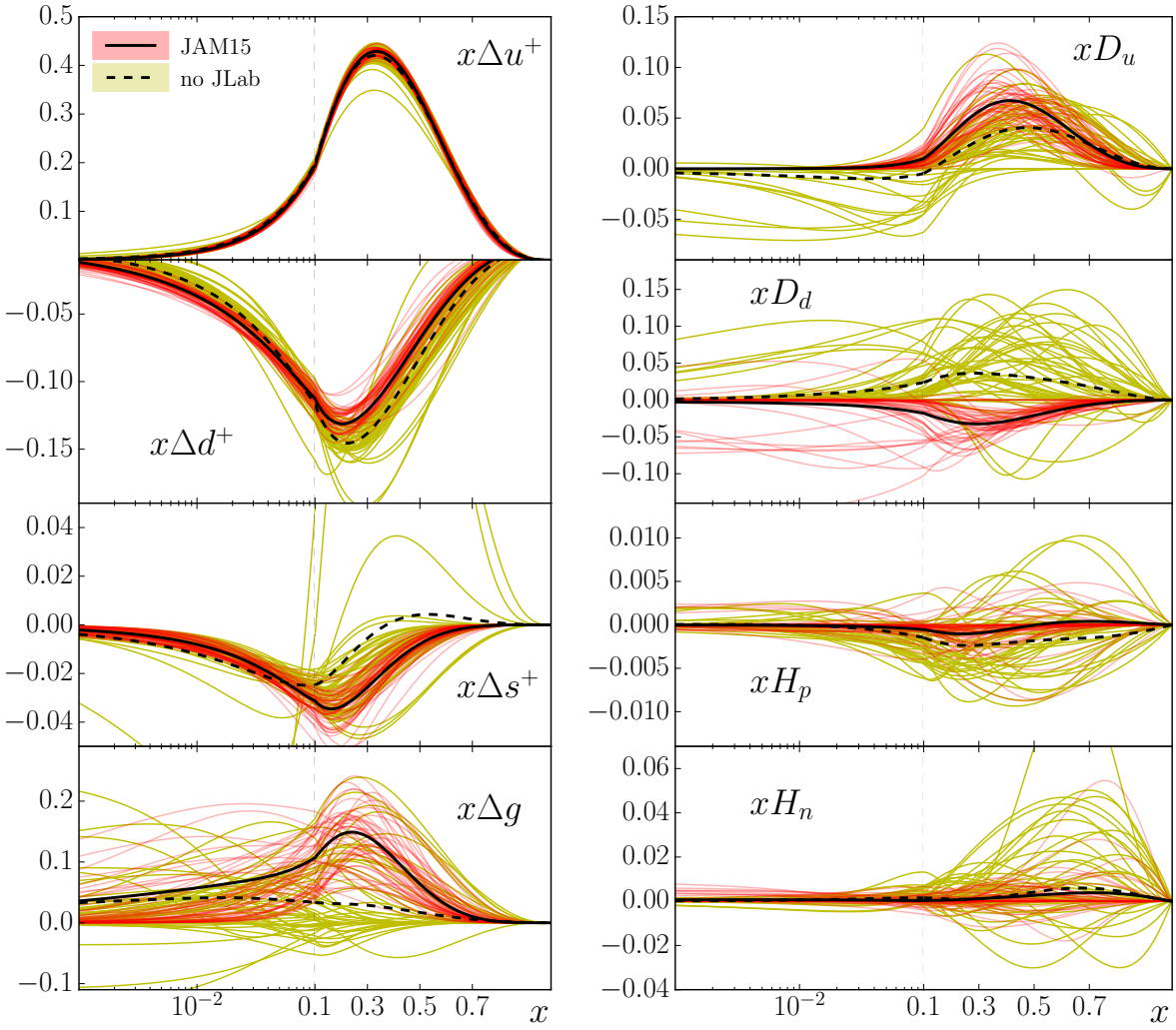

FIG. 15: Comparison of the JAM15 IMC fits (red curves, with the average indicated by the black solid curve) with corresponding fits excluding all Jefferson Lab data (yellow curves, with the average given by the black dashed curve) for the twist-2 PDFs Δu^+, Δd^+, Δs^+ and Δg, the twist-3 distributions D_u and D_d, and the twist-4 functions H_p and H_n at $Q^2 = 1$ GeV^2. Note that x times the distribution is shown. For illustration each distribution is represented by a random sample of 50 fits.

8000 fits, for clarity in Fig. 15 we illustrate the results by a random sample of 50 fits.

The inclusion of the Jefferson Lab data results in a reduction of the uncertainty bands on the Δu^+ and Δd^+ PDFs in the region $0.1 \lesssim x \lesssim 0.7$ where the Jefferson Lab data are localized. This may be expected given that these distributions give the leading contributions to the inclusive DIS asymmetries at these kinematics.

Interestingly, however, we also observe significant reduction of the uncertainties in Δu^+ and Δd^+ at small values of x, outside of the kinematic range of the Jefferson Lab experiments. By studying the correlations between PDFs over the entire x range, which are partly induced by the weak baryon decay constraints [Eqs. (38) and (39)], we find a strong anticorrelation between the Δu^+ distribution at large and small x values. Since the Jefferson Lab data tend to favor a higher Δu^+ in the region $0.1 \lesssim x \lesssim 0.7$, the anticorrelation has the effect of favoring a suppressed Δu^+ at low x. Similar arguments hold also for Δd^+ PDF.

In the absence of Jefferson Lab data, a strong correlation also exists between higher values of the polarized strange PDF Δs^+ at $x \sim 0.4$ and higher Δu^+ at small x. The disfavoring by the data of the latter then indirectly constrains the strange distribution to have smaller values across all x. The uncertainty on Δs^+ is also significantly larger without the Jefferson Lab constraints, as indicated by the larger spread of the fitted results in Fig. 15. The strange quark distribution illustrates the point that in the Monte Carlo approach there is no guarantee that the final posteriors will be clustered in a specific region of parameter space. For example, two distinct solutions can describe the same PDF in some neighborhood of x, while deviating in other x regions; data cannot distinguish the two solutions due to correlations. Such a picture of multiple regions and error bands is absent in traditional single-fit analyses, where the effect of adding more data means that the χ^2 is steeper around the minimum. While this is also true for Monte Carlo fits, in the IMC approach, however, the error bands in practice cover more than one minimium, if multiple solutions are present.

The Δs^+ PDF is also indirectly impacted by the different Q^2 evolution of the singlet and nonsinglet distributions, especially with the greater statistics at lower Q^2 values afforded by the Jefferson Lab data. The Q^2 evolution also provides a way of indirectly constraining the polarized gluon distribution Δg, in the absence of jet data from polarized pp collisions [5] in the current analysis. Indeed, as Fig. 15 indicates, the new Jefferson Lab results actually prefer a more positive Δg distribution at intermediate x values, $x \approx 0.1 - 0.5$, with a smaller spread of possible behaviors, but with still large uncertainties at lower x.

In the higher twist sector, as one might expect, the greater abundance of lower-Q^2 data provides even more stringent constraints on the twist-3 and twist-4 distributions. In particular, the global analysis reveals that with the addition of Jefferson Lab data the twist-3 D_u distribution becomes more positive at $x > 0.1$, while the D_d distribution effectively switches sign to become negative and smaller in magnitude. The twist-3 distributions thus acquire

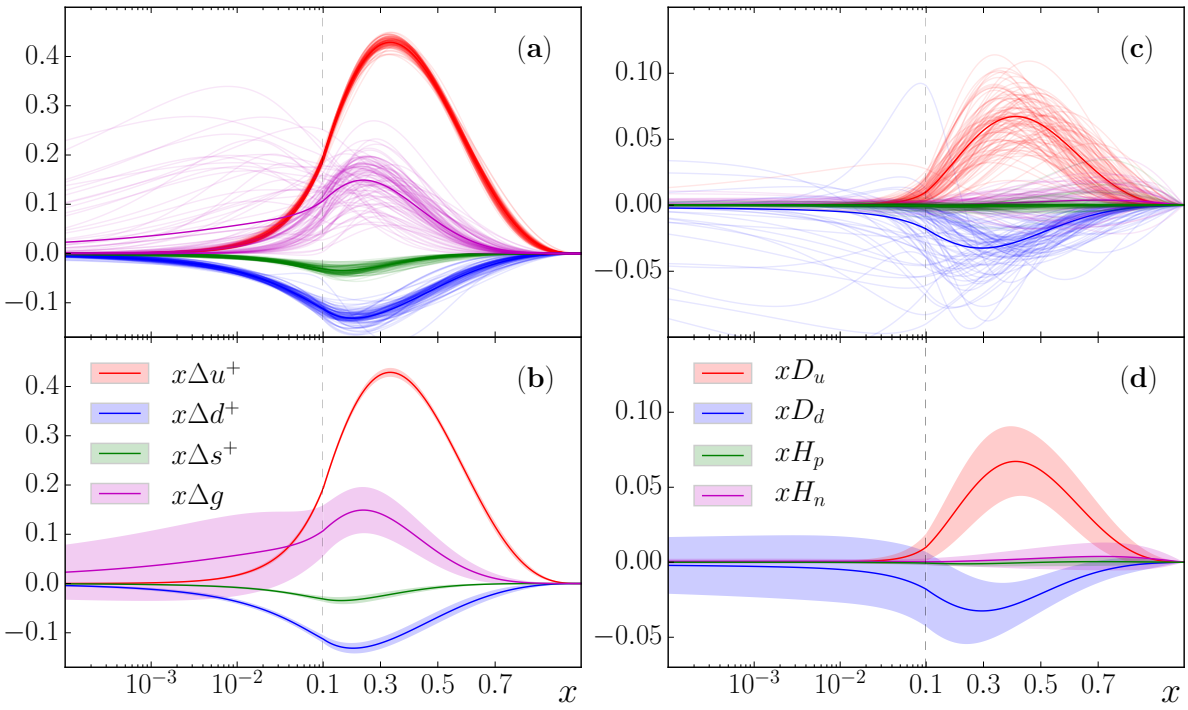

FIG. 16: Leading twist Δu^+, Δd^+, Δs^+ and Δg distributions [**(a)** and **(b)**] and the higher twist $D_{u,d}$ and $H_{p,n}$ distributions [**(c)** and **(d)**] as a function of x for $Q^2 = 1$ GeV^2. Panels **(a)** and **(c)** show a random sample of 100 from the 8000 IMC fits, while **(b)** and **(d)** show the average distributions and the standard deviations computed from Eqs. (47) and (48). Note that x times the distribution is shown.

the same signs for the u and d flavors as their twist-2 PDF analogs.

For the twist-4 distributions, while H_p and H_n are largely unconstrained in the fit without Jefferson Lab data, in the full fit the spread is reduced considerably, and the results for both distributions are consistent with zero. The dominant contributions of the higher twists to the DIS asymmetries are therefore driven by the twist-3 terms.

D. JAM15 distributions and moments

The final distributions for the full JAM15 fit are displayed in Fig. 16 as a function of x at fixed $Q^2 = 1$ GeV^2, with the leading twist PDFs and the higher twist distributions for different flavors shown on the same graph for comparison. To illustrate the Monte Carlo aspect of the analysis, a random selection of 100 fits from the full sample of $\approx$ 8000 in

TABLE IV: Lowest moments of the twist-2 PDFs Δu^+, Δd^+, Δs^+, $\Delta\Sigma$ and ΔG, the twist-3 d_2^p and d_2^n moments, and the x^2-weighted moments h_p and h_n of the twist-4 distributions. The truncated moments in the measured region $x \in [0.001, 0.8]$ and the extrapolated full moments are shown at $Q^2 = 1$ GeV^2.

moment	truncated	full
Δu^+	0.82 ± 0.01	0.83 ± 0.01
Δd^+	-0.42 ± 0.01	-0.44 ± 0.01
Δs^+	-0.10 ± 0.01	-0.10 ± 0.01
$\Delta\Sigma$	0.31 ± 0.03	0.28 ± 0.04
ΔG	0.5 ± 0.4	1 ± 15
d_2^p	0.005 ± 0.002	0.005 ± 0.002
d_2^n	-0.001 ± 0.001	-0.001 ± 0.001
h_p	-0.000 ± 0.001	0.000 ± 0.001
h_n	0.001 ± 0.002	0.001 ± 0.003

the full analysis is shown, along with the expectation values and standard deviations for each distribution computed from Eqs. (47) and (48) using the full sample. The Δu^+ and Δd^+ PDFs are the best determined distributions from the inclusive DIS data, with relatively small uncertainty bands. We stress that the uncertainties here are computed unambiguously from the Monte Carlo analysis, independent of any tolerance criteria, which are sometimes invoked in single-fit analyses to inflate PDF errors when fitting incompatible data sets [3]. Integrated over all x, the lowest moments of the Δu^+ and Δd^+ distributions are 0.83 ± 0.01 and -0.42 ± 0.01, respectively. The contributions from the extrapolated regions, $x < 0.001$ and $x > 0.8$, where the PDFs are not directly constrained by data, are very small as a comparison between the truncated and full moments in Table IV demonstrates.

The strange quark distribution Δs^+ turns out to be negative, constrained by a combination of Q^2 evolution, weak baryon decay constants, and the assumption of an SU(3) symmetric sea, Eq. (37). The value of Δs^+ integrated over x is -0.10 ± 0.01, which then implies a total helicity carried by quarks and antiquarks of $\Delta\Sigma = 0.28 \pm 0.04$ at the input

scale. The extrapolated region contributes little to the moments of the quark distributions, in contrast to the gluon case, where the unmeasured region plays a much more important role. In particular, while the gluon helicity from the experimentally constrained region is 0.5 ± 0.4, the total moment approximately doubles in magnitude, but with a significantly larger uncertainty, $\Delta G = 1 \pm 15$. This is reflected by the much wider error band on the $\Delta g(x)$ distribution in Fig. 16 than on the polarized quark PDFs. The uncertainty is expected to be reduced once jet and pion production data from polarized pp collisions are included in the analysis [40].

The difficulty in constraining the polarized gluon distribution is clearly revealed through the spread of Δg from various global PDF parametrizations illustrated in Fig. 17. Here the PDFs from the DSSV09 [21], AAC09 [24], BB10 [22], LSS10 [23] and NNPDF14 [28] global analyses are compared with the JAM15 results, and with the previous JAM13 [20] distributions. Note that the BB10 fit uses only inclusive DIS data, similar to our analysis and JAM13, while LSS10 includes also semi-inclusive DIS asymmetries. The other analyses consider in addition data from polarized pp scattering with jet and π production at RHIC, which have the strongest constraints on the gluon polarization, while NNPDF14 also includes W boson asymmetries to constrain the antiquark sea.

In most of the fits the Δg PDF is positive at large x, with a sign change at smaller x values for the DSSV09, BB10 and NNPDF14 PDFs. Even though a node is allowed in the JAM15 parametrization, our analysis with inclusive DIS data only does not favor a sign change. Depending on which data sets are included in the fits, the integrated gluon moment ΔG can vary enormously between the parametrizations. Interestingly, the latest analysis by de Florian *et al.* [9] of the recent high-statistics jet data from RHIC also gives a positive Δg distribution, qualitatively similar to the JAM15 result, with no indication of a sign change in the measured x region.

The sign of the Δs^+ distribution is consistent with that found in previous global PDF analyses based on inclusive DIS data, as Fig. 17 illustrates. As a function of x, the shape of the JAM15 Δs^+ is slightly harder than for other PDF parametrizations, which stems from the inclusion of the Jefferson Lab Hall B data [14, 15] and the correlations with the polarized u and d distributions (see below). A softer polarized strange distribution could be obtained by enforcing a larger value for the b parameter in Eq. (35), as is assumed in many of the single-fit PDF analyses. In our IMC analysis we allow the strange quark b parameter in the

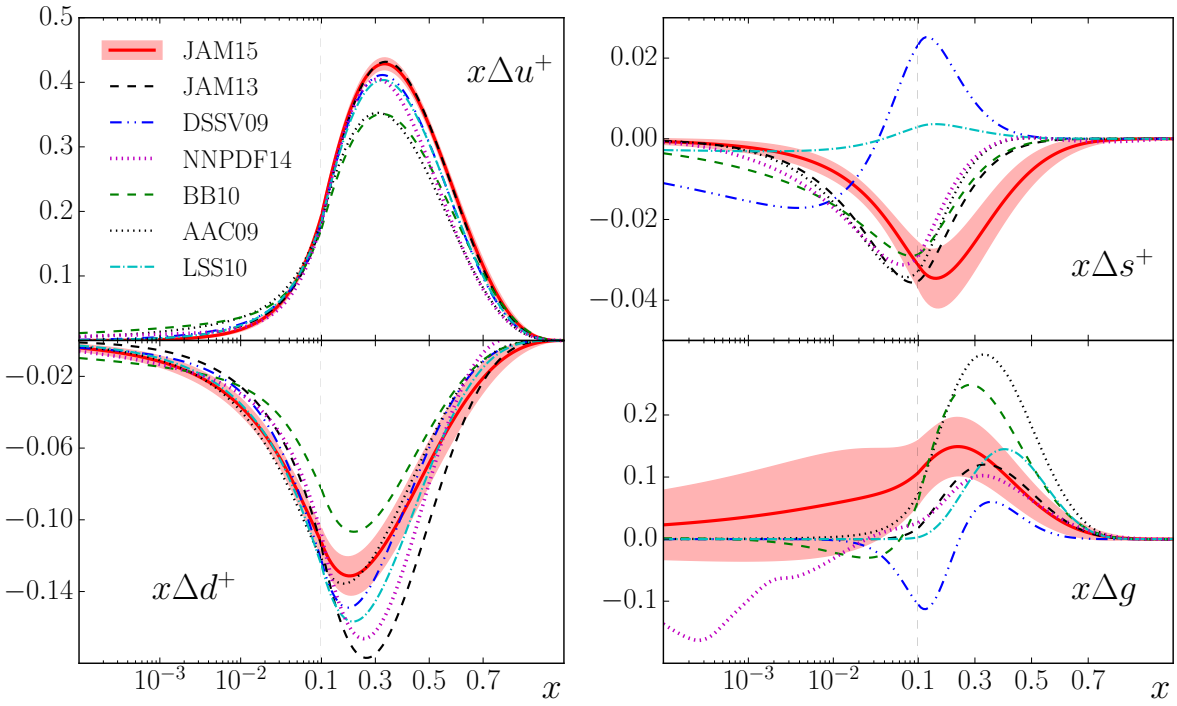

FIG. 17: Comparison of the JAM15 PDFs Δu^+, Δd^+, Δs^+ and Δg at $Q^2 = 1$ GeV^2 with PDFs from other parametrizations in the literature, including DSSV09 [21], NNPDF14 [28], BB10 [22], AAC09 [24], LSS10 [23], and JAM13 [20].

initial sampling to be as large as 10; however, the Monte Carlo fits prefer smaller values. In contrast to the negative Δs^+ obtained from the analysis of DIS asymmetries, inclusion of the semi-inclusive kaon production data in the DSSV09 and LSS10 fits induces a positive Δs^+ at $x \gtrsim 0.05$. Currently the tension between the inclusive and semi-inclusive DIS data and their impact on the sign of the polarized strange distribution is not completely understood [88, 89], and the definitive extraction of Δs^+ will require careful treatment of all processes to which strange quarks contribute, as well as a reliable determination of fragmentation functions.

For the much better determined Δu^+ and Δd^+ distributions, the shapes and magnitudes from the JAM15 fit are generally similar to those found in previous analyses, but with some important features. The Δu^+ PDF is slightly higher at intermediate $x \approx 0.3 - 0.5$ than in most of the other analyses, as was the case for the JAM13 distribution, but overall the spread between the different parametrizations is relatively small. The BB10 and AAC09 Δu^+ distributions have the smallest magnitude at the peak, $\approx 20\%$ smaller than JAM15.

The Δd^+ distribution, on the other hand, is somewhat less negative at $x \gtrsim 0.1$ than the JAM13 result, but similar to the DSSV09 and AAC09 distributions. Interestingly, the JAM15 Δd^+ PDF is also similar to the "reference" fit from the JAM13 analysis [20], which did not include any nuclear smearing or finite-Q^2 corretions. As shown in Ref. [20], nuclear smearing and higher twist corrections in particular render Δd^+ more negative for $x \gtrsim 0.2$. Inclusion of the new Jefferson Lab data make Δd^+ less negative, countering the effects of the nuclear and hadronic corrections. Because of the weak baryon constraints on the moments of the quark PDFs, many aspects of the Δu^+, Δd^+ and Δs^+ distributions and their uncertainties are strongly correlated. Compared with the JAM13 distributions, for example, the shift in the JAM15 Δd^+ PDF towards more positive values at $x \gtrsim 0.2$ is directly correlated with the shift of the Δs^+ toward more negative values at similar x, to allow a similar quality fit to the observables. In this respect the flavor singlet moment $\Delta\Sigma$ is relative stable between the different fits, with central values ranging from 0.24 in the NNPDF14 analysis [28] to 0.34 in the BB10 fit [22] at $Q^2 = 1$ GeV^2.

In the higher twist sector, as indicated in Fig. 15, the twist-3 distributions D_u and D_d acquire unambiguous positive and negative signs, respectively, at large x values, with magnitudes clearly different from zero. Of most physical interest are the x^2-weighted moments of D_u and D_d, which we find to be $\boldsymbol{D}_u(3, Q^2) = 0.013 \pm 0.005$ and $\boldsymbol{D}_d(3, Q^2) = -0.005 \pm 0.003$ at $Q^2 = 1$ GeV^2. Taking the appropriate charge squared-weighted combination of these, one finds that for the proton the twist-3 contribution is large, while for the neutron it mostly cancels. This correlates with the larger higher twist effects observed for the proton asymmetries at low Q^2 in Figs. 8 and 9 than in the corresponding asymmetries for ^{3}He ("neutron"), and to some extent also the deuteron.

The moments h_p and h_n of the twist-4 distributions are all compatible with zero, for both the truncated and full moments. This observation gives confidence that the twist-3 PDFs, and consequently the d_2 moments, in our analysis are determined reliably, without significant contamination from subleading contributions of higher twist.

The Q^2 dependence of the d_2 moments for the proton and neutron from the JAM15 analysis is presented in Fig. 18(a) for Q^2 between 1 and 5 GeV^2. Note that the quoted JAM15 d_2 values contain only twist-3 contributions, without TMCs [see Eq. (24)], while the corresponding experimental moments in principle contain contributions beyond twist-3 as well as target mass effects. For ease of notation, we will omit the explicit label "(τ3)"

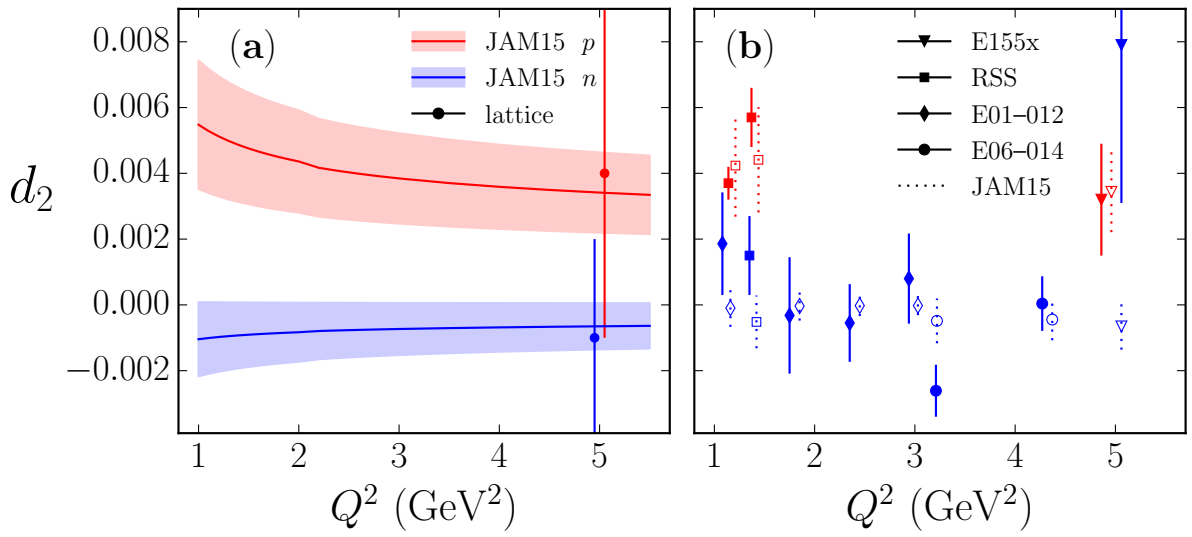

FIG. 18: d_2 moments of the proton and neutron computed from the JAM15 twist-3 D_u and D_d distributions and compared with **(a)** lattice QCD calculations [90], and **(b)** moments extracted from the g_1 and g_2 structure functions from several SLAC [81] and Jefferson Lab [18, 19, 91, 92] experiments (filled symbols), with the JAM15 results (open symbols) corresponding to the experimentally measured regions. The E155x results include extrapolations into unmeasured regions at low and high x, while the Jefferson Lab results are mostly from the resonance region.

from the JAM15 d_2 moments in the following. As expected from the values for the D_u and D_d moments discussed above, the proton d_2^p moment is positive and 1–2 σ away from zero, decreasing gradually from its value $d_2^p = 0.005 \pm 0.002$ at $Q^2 = 1$ GeV^2 with increasing Q^2. The neutron d_2^n moment, on the other hand, is negative and much smaller in magnitude, but consistent with zero within the uncertainties, $d_2^n = -0.001 \pm 0.001$. Remarkably, without the new Jefferson Lab data, the values of d_2 extracted from the global analysis (yellow curves in Fig. 15) would be 0.005 ± 0.002 for the proton and 0.005 ± 0.005 for the neutron. Thus, while the proton d_2 moment is essentially unchanged, the neutron central value changes sign, although still consistent with zero. This effect is mostly driven by the new ^{3}He data from Hall A [17, 18]. The results in Fig. 18 therefore represent the most reliable determination of the twist-3 d_2 moments in global QCD analyses to date.

Our extracted d_2 values can also be compared with first principles calculations of the d_2 matrix elements of local twist-3 operators in lattice QCD. In their simulations, the QCDSF/UKQCD Collaboration found $d_2^p = 0.004(5)$ and $d_2^n = -0.001(3)$ at a scale of

TABLE V: d_2 moments of the proton and neutron $g_{1,2}$ structure functions from the SLAC E155x [81] and Jefferson Lab RSS [91, 92], E01-012 [19] and E06-014 [18] experiments, compared with the d_2 moments computed from the JAM15 twist-3 $D_{u,d}$ distributions. The Q^2 values and the W and x ranges for each experiment are given. The E155x d_2 values include extrapolations into unmeasured regions, while the others are truncated moments over the measured regions only. The errors on the JAM15 values are given to the relevant number of significant figures, while the experimental results are quoted from the respective publications.

experiment	ref.	target	Q^2 (GeV^2)	W range (GeV)	x range	d_2(JAM15)	d_2(exp.)
E155x	[81]	p	5.00	$> M$	[0, 1]	0.003(1)	0.0032(17)
	[81]	n	5.00	$> M$	[0, 1]	−0.0007(7)	0.0079(48)
RSS	[91]	p	1.30	[1.06, 2.01]	[0.29, 0.84]	0.004(2)	0.0057(9)
	[92]	p	1.28	[1.08, 1.91]	[0.32, 0.82]	0.004(2)	0.0037(5)
	[92]	n	1.28	[1.08, 1.91]	[0.32, 0.82]	−0.0005(8)	0.0015(12)
E01-012	[19]	n	1.20	[1.04, 1.38]	[0.54, 0.86]	−0.0001(6)	0.00186(156)
	[19]	n	1.80	[1.09, 1.56]	[0.54, 0.86]	0.0000(4)	−0.00032(177)
	[19]	n	2.40	[1.07, 1.50]	[0.64, 0.90]	0.0000(3)	−0.00055(118)
	[19]	n	3.00	[1.10, 1.61]	[0.64, 0.90]	0.0000(3)	0.00080(137)
E06-014	[18]	n	3.21	[1.11, 3.24]	[0.25, 0.90]	−0.0005(7)	−0.00261(79)
	[18]	n	4.32	[1.17, 3.72]	[0.25, 0.90]	−0.0005(6)	0.00004(83)

$Q^2 = 5$ GeV^2 [90], which agrees well with the JAM15 values, as Fig. 18(a) demonstrates.

Comparisons with d_2 moments extracted from the g_1 and g_2 structure functions measured in several SLAC and Jefferson Lab experiments are illustrated in Fig. 18(b) and listed in Table V. In the case of the SLAC E155x experiment, the d_2 values are extrapolated from the measured region to $x = 0$ and $x = 1$, while in the Jefferson Lab experiments only the truncted moments over the measured regions are reported. With the exception of the E06-014 data [18], which partially extend into the DIS region, the truncated moments for the Jefferson Lab experiments [19, 91, 92] are restricted entirely to the nucleon resonance region. Note that we do not include the nucleon elastic contribution in any of the experimental or

theoretical moments. Agreement between the purely resonant empirical contributions to d_2 and the twist-3 truncated moments from the JAM15 PDFs would therefore imply the validity of quark-hadron duality for the twist-3 spin distribution functions. Conversely, any differences between these may be interpreted as a violation of duality [93].

In fact, most of the experimental points for both protons and neutrons show reasonable agreement with the JAM15 d_2 values within the experimental and PDF errors. An exception is the lower-Q^2 point from Jefferson Lab E06-014, which is about 2σ lower than the JAM15 result, and the SLAC E155x neutron value at $Q^2 = 5$ GeV^2, which is significantly higher (albeit with sizable uncertainty) than any of the other neutron d_2 results at lower Q^2 and the JAM15 fit. Future data from Jefferson Lab at 12 GeV [94] may enable the neutron d_2 moment to be determined more precisely up to $Q^2 \approx 6$ GeV^2.

VI. CONCLUSION

We have performed a new global QCD analysis of spin-dependent parton distributions including all available inclusive DIS data on longitudinal and transverse polarization asymmetries from experiments at CERN, SLAC and DESY, and new high-precision measurements from Jefferson Lab. The analysis is the first performed using a newly developed fitting strategy based on data resampling and cross validation, the key feature of which is the iterative methodology. This approach is fundamentally data-driven, with the prior parameters that are initially distributed from flat sampling across parameter space iteratively transformed into posteriors that are distributed consistently with the information contained in the data and its uncertainties.

One of the main advantages of the iterative Monte Carlo approach is that by sampling over a large parameter space one can avoid introducing biases that are inherent in standard single-fit analyses that assume a specific set of initial fitting parameters. Since the χ^2 is a highly nonlinear function of the fit parameters, in the presence of multiple solutions any single fit can be stuck in a local minimum and yield unreliable results for the PDFs. This is particularly relevant for the higher twist distributions, for which there is considerably less experience in global fitting. Furthermore, being based on statistical error analysis, the IMC procedure allows for the unambiguous determination of PDF errors, without the need for introducing any tolerance criteria when handling numerous data sets.

Our aim has been to maximally utilize the available data over the greatest range of kinematics which the theoretical perturbative QCD description permits. To this end we evaluate both the longitudinal and transverse asymmetries consistently up to $\mathcal{O}(1/Q^2)$ corrections, which necessitates including twist-3 and twist-4 contributions to the g_1 structure function and twist-3 corrections to g_2, as well as the known target mass corrections to the leading twist and twist-3 terms. In addition, we account for nuclear smearing effects, including finite-Q^2 corrections to these, for data on deuterium and ^{3}He targets, which constitutes about 1/3 of the total data base. To empirically determine the optimal kinematic range over which the data can be reliably fitted, we studied the sensitivity of the results to the choice of cuts on W^2 and Q^2. By examining the stability of the moments of the extracted PDFs with respect to the cuts, we could ascertain that the limits $W^2_{\rm cut} = 4$ GeV^2 and $Q^2_{\rm cut} = 1$ GeV^2 correspond to the boundary of the applicability of the current global analysis.

Overall a very good description of the global inclusive DIS data set has been obtained in our fit, over the entire range of Q^2 and x covered by the preferred cuts. Of the approximately 2500 data points in the global data set, around 1400 have been added with the inclusion of the new high-precision Jefferson Lab data, especially at lower Q^2 and W^2. The impact of the new data has been a general reduction of the uncertainties on the leading twist and higher twist distributions in the measured region.

For the Δu^+ and Δd^+ distributions, the new PDFs are qualitatively similar to those found in previous global analyses, with Δu^+ slightly higher at intermediate x values, while Δd^+ is somewhat less negative at large $x \gtrsim 0.1$ than in the previous JAM13 fit [20]. One of the limitations of the inclusive DIS-only analysis is the introduction of large correlations between the nonstrange and strange quark PDFs, which results in a slightly harder Δs^+ distribution, but one which has a clear negative sign. Furthermore, with the addition of the lower-Q^2 Jefferson Lab data, the gluon distribution, which is constrained here mainly through Q^2 evolution, becomes positive across all x values, and is remarkably similar to the latest fit from Ref. [9] that includes the recent RHIC jet data.

The biggest impact of the Jefferson Lab data, however, is in the higher twist sector, where the new high-precision asymmetries on the proton and deuteron from CLAS in Hall B [14–16] and on ^{3}He from Hall A [17, 18] allow the flavor dependence of the twist-3 distributions D_u and D_d to be determined. In particular, we find that the sign of the D_d PDF changes from positive to negative, which directly impacts the determination of the twist-3 d_2 moments

of the neutron. Thus while the proton d_2^p moment remains large (on the scale of previous measurements) and positive, the new neutron d_2^n moment becomes negative, although still compatible with zero to within 1σ. Interestingly, the JAM15 d_2 results agree well with the available lattice QCD calculations at $Q^2 = 5$ GeV^2 [90] for both the proton and neutron, but disagree with the magnitude and sign of the neutron d_2^n moment extracted from the SLAC E155x experiment [81].

In the future, data from 12 GeV Jefferson Lab experiments will allow the d_2 moments to be determined more precisely in the DIS region at higher Q^2 values [94], and also provide stronger constraints on the large-x behavior of PDFs through precise measurements of polarization asymmetries over a greater range of Q^2 and W^2 [95, 96]. In the shorter term, the current analysis will be extended to include semi-inclusive DIS asymmetries, which will place stronger constraints on the sea quark polarization, as well as jet and π production asymmetries in polarized pp collisions [40]. In view of the importance of determining the proton spin decomposition into its constituent components, it will be of great interest to explore the emergent picture for the sea quark and gluon polarization within the IMC approach.

Acknowledgement

We are grateful to M. Stratmann and W. Vogelsang for assistance with Mellin moment techniques, and to C. Fernández-Ramírez, P. Jimenez-Delgado, F. M. Steffens and the experimental members of the JAM Collaboration [97] for helpful discussions. This work was supported by the US Department of Energy (DOE) contract No. DE-AC05-06OR23177, under which Jefferson Science Associates, LLC operates Jefferson Lab. A.A. was partially supported by the DOE contract No. DE-SC008791, S.K. was supported by the DOE under contract DE-FG02-96ER40960, and N.S. was partially supported by GAUSTEQ (Germany and U.S. Nuclear Theory Exchange Program for QCD Studies of Hadrons and Nuclei), DOE contract No. DE-SC0006758.

Appendix A: Notations

In this appendix we provide for convenience a summary of the notations used in this work for several common moments of twist-2, twist-3 and twist-4 distributions. In general, we define the N-th Mellin moment of a function $f(x)$ by

$$\boldsymbol{f}(N,Q^2) = \int_0^1 dx\, x^{N-1}\, f(x,Q^2), \tag{A1}$$

which is a continuous functions of N. To distiniguish the moments $\boldsymbol{f}(N,Q^2)$ from the x-dependent distributions $f(x,Q^2)$, we denote these in boldface. Table VI summarizes the different notations used according to Eq. (A1) here and elsewhere in the literature.

TABLE VI: Summary of notations used in this work for some moments of twist-2, twist-3 and twist-4 distributions, including the formal notation as defined in Eq. (A1) and the definitions in terms of integrals of PDFs and structure functions.

shorthand	formal	definition
$\Delta\Sigma(Q^2)$	$\sum_q \boldsymbol{\Delta q}^+(1,Q^2)$	$\sum_q \int_0^1 dx\ \Delta q^+(x,Q^2)$
$\Delta G(Q^2)$	$\boldsymbol{\Delta g}(1,Q^2)$	$\int_0^1 dx\ \Delta g(x,Q^2)$
$d_2(Q^2)$	$2\boldsymbol{g}_1(3,Q^2) + 3\boldsymbol{g}_2(3,Q^2)$	$\int_0^1 dx\, x^2\, [2g_1(x,Q^2) + 3g_2(x,Q^2)]$
$d_2^{(\tau 3)}(Q^2)$	$2\boldsymbol{g}_1^{(\tau 3)}(3,Q^2) + 3\boldsymbol{g}_2^{(\tau 3)}(3,Q^2)$	$\int_0^1 dx\, x^2\, [2g_1^{(\tau 3)}(x,Q^2) + 3g_2^{(\tau 3)}(x,Q^2)]$
	$= \sum_q\ e_q^2\ \boldsymbol{D}_q(3,Q^2)$	
$h(Q^2)$	$\boldsymbol{H}(3,Q^2)$	$\int_0^1 dx\ x^2\ H(x,Q^2)$

[1] B. Lampe and E. Reya, Phys. Rep. **332**, 1 (2000).

[2] C. A. Aidala, S. D. Bass, D. Hasch and G. K. Mallot, Rev. Mod. Phys. **85**, 655 (2013).

[3] P. Jimenez-Delgado, W. Melnitchouk and J. F. Owens, J. Phys. G: Nucl. Part. Phys. **40**, 093102 (2013).

[4] E. Leader and C. Lorcé, Phys. Rep. **541**, 163 (2014).

[5] L. Adamczyk *et al.*, Phys. Rev. Lett. **115**, 092002 (2015).

[6] A. Adare *et al.*, Phys. Rev. D **90**, 012007 (2014).

[7] A. Adare *et al.*, arXiv:1510.02317 [hep-ex].

[8] C. Adolph *et al.*, Phys. Rev. D **87**, 052018 (2013).

[9] D. de Florian, R. Sassot, M. Stratmann and W. Vogelsang, Phys. Rev. Lett. **113**, 012001 (2014).

[10] L. Adamczyk *et al.*, Phys. Rev. Lett. **113**, 072301 (2014).

[11] A. Adare *et al.*, arXiv:1504.07451 [hep-ex].

[12] K. V. Dharmwardane *et al.*, Phys. Lett. B **641**, 11 (2006).

[13] Y. Prok *et al.*, Phys. Lett. B **672**, 12 (2009).

[14] R. G. Fersch, N. Guler, P. Bosted, A. Deur, K. Griffioen, S. E. Kuhn, R. Minehart, Y. Prok *et al.* [CLAS Collaboration]: "Precise determination of proton spin structure functions at low to moderate Q^2 with CLAS", to be published in Phys. Rev. C (2016).

[15] Y. Prok *et al.*, Phys. Rev. C **90**, 025212 (2014).

[16] N. Guler *et al.*, Phys. Rev. C **92**, 055201 (2015).

[17] D. S. Parno *et al.*, Phys. Lett. B **744**, 309 (2015).

[18] M. Posik *et al.*, Phys. Rev. Lett. **113**, 022002 (2014).

[19] P. Solvignon *et al.*, Phys. Rev. C **92**, 015208 (2015).

[20] P. Jimenez-Delgado, A. Accardi and W. Melnitchouk, Phys. Rev. D **89**, 034025 (2014).

[21] D. de Florian, R. Sassot, M. Stratmann and W. Vogelsang, Phys. Rev. D **80**, 034030 (2009).

[22] J. Blümlein and H. Böttcher, Nucl. Phys. **B841**, 205 (2010).

[23] E. Leader, A. V. Sidorov and D. B. Stamenov, Phys. Rev. D **82**, 114018 (2010).

[24] M. Hirai and S. Kumano, Nucl. Phys. **B813**, 106 (2009).

[25] F. Arbabifar, A. N. Khorramian and M. Soleymaninia, Phys. Rev. D **89**, 034006 (2014).

[26] A. Accardi, A. Bacchetta, W. Melnitchouk and M. Schlegel, JHEP **0911**, 093 (2009).

[27] J. Blümlein and H. Böttcher, in Proceedings, 20th International Workshop on Deep-Inelastic Scattering and Related Subjects (DIS 2012), Bonn, Germany, March 26-30, 2012; arXiv:1207.3170 [hep-ph].

[28] E. R. Nocera *et al.*, Nucl. Phys. **B887**, 276 (2014).

[29] S. A. Kulagin and W. Melnitchouk, Phys. Rev. C **77**, 015210 (2008).

[30] S. A. Kulagin and W. Melnitchouk, Phys. Rev. C **78**, 065203 (2008).

[31] J. J. Ethier and W. Melnitchouk, Phys. Rev. C **88**, 054001 (2013).

[32] S. Wandzura, Nucl. Phys. **B122**, 412 (1977).

[33] J. Blümlein and A. Tkabladze, Nucl. Phys. **B553**, 427 (1999).

[34] S. Matsuda and T. Uematsu, Nucl. Phys. **B168**, 181 (1980).

[35] A. Piccione and G. Ridolfi, Nucl. Phys. **B513**, 301 (1998).

[36] A. Accardi and W. Melnitchouk, Phys. Lett. B **670**, 114 (2008).

[37] V. M. Braun, G. P. Korchemsky and A. N. Manashov, Nucl. Phys. **B603**, 69 (2001).

[38] V. M. Braun, A. N. Manashov and B. Pirnay, Phys. Rev. D **80**, 114002 (2009).

[39] C. Adolph *et al.*, Phys. Lett. B **753**, 18 (2016).

[40] N. Sato *et al.*, in preparation (2016).

[41] S. Wandzura and F. Wilczek, Phys. Lett. B **72**, 195 (1977).

[42] H. Burkhardt and W. N. Cottingham, Annals Phys. **56**, 453 (1970).

[43] O. Nachtmann, Nucl. Phys. **B63**, 237 (1973).

[44] O. W. Greenberg and D. Bhaumik, Phys. Rev. D **4**, 2048 (1971).

[45] H. Georgi and H. D. Politzer, Phys. Rev. D **14**, 1829 (1976).

[46] A. De Rújula, H. Georgi and H. D. Politzer, Annals Phys. **103**, 315 (1977).

[47] A. De Rújula, H. Georgi and H. D. Politzer, Phys. Rev. D **15**, 2495 (1977).

[48] K. Bitar, P. W. Johnson, and W.-K. Tung, Phys. Lett. B **83**, 114 (1979).

[49] F. M. Steffens and W. Melnitchouk, Phys. Rev. C **73**, 055202 (2006).

[50] I. Schienbein *et al.*, J. Phys. G **35**, 053101 (2008).

[51] F. M. Steffens, M. D. Brown, W. Melnitchouk and S. Sanches, Phys. Rev. C **86**, 065208 (2012).

[52] A. Accardi and J. W. Qiu, JHEP **07**, 090 (2008).

[53] X. Ji and W. Melnitchouk, Phys. Rev. D **56**, 1 (1997).

[54] A. Deur *et al.*, Phys. Rev. Lett. **93**, 212001 (2004).

[55] M. Osipenko, W. Melnitchouk, S. Simula *et al.*, Phys. Lett. B **609**, 259 (2005).

[56] Z.-E. Meziani, W. Melnitchouk, J.-P. Chen, S. Choi *et al.*, Phys. Lett. B **613**, 148 (2005).

[57] R. L. Jaffe and X. D. Ji, Phys. Rev. D **43**, 724 (1991).

[58] X. Ji and P. Unrau, Phys. Lett. B **333**, 228 (1994).

[59] E. Stein, P. Gornicki, L. Mankiewicz, A. Schafer and W. Greiner, Phys. Lett. B **343**, 369 (1995).

[60] E. Stein, P. Gornicki, L. Mankiewicz and A. Schafer, Phys. Lett. B **353**, 107 (1995).

[61] M. Burkardt, Phys. Rev. D **88**, 114502 (2013).

[62] J. F. Owens, A. Accardi and W. Melnitchouk, Phys. Rev. D **87**, 094012 (2013).

[63] A. Vogt, Comput. Phys. Commun. **170**, 65 (2005).

[64] S. Alekhin, S. A. Kulagin and R. Petti, AIP Conf. Proc. **967**, 215 (2007).

[65] L. T. Brady, A. Accardi, T. J. Hobbs and W. Melnitchouk, Phys. Rev. D **84** (2011) 074008 [Phys. Rev. D **85** (2012) 039902].

[66] M. Stratmann and W. Vogelsang, Phys. Rev. D **64**, 114007 (2001).

[67] G. D'Agostini, Nucl. Instrum. Meth. A **346**, 306 (1994).

[68] J. J. More, B. S. Garbow and K. E. Hillstrom, it User Guide for Minpack-1, ANL-80-74.

[69] J. Ashman *et al.*, Nucl. Phys. **B328**, 1 (1989).

[70] B. Adeva *et al.*, Phys. Rev. D **58**, 112001 (1998).

[71] B. Adeva *et al.*, Phys. Rev. D **60**, 072004 (1999);

[72] M. G. Alekseev *et al.*, Phys. Lett. B **690**, 466 (2010).

[73] V. Yu. Alexakhin *et al.*, Phys. Lett. B **647**, 8 (2007).

[74] G. Baum *et al.*, Phys. Rev. Lett. **51**, 1135 (1983).

[75] P. L. Anthony *et al.*, Phys. Rev. D **54**, 6620 (1996).

[76] K. Abe *et al.*, Phys. Rev. D **58**, 112003 (1998).

[77] K. Abe *et al.*, Phys. Rev. Lett. **79**, 26 (1997); Yu. Kolomensky, Ph.D. thesis, U. Massachusetts (1997), SLAC-Report-503.

[78] P. L. Anthony *et al.*, Phys. Lett. B **493**, 19 (2000); O. A. Rondon, private communication.

[79] P. L. Anthony *et al.*, Phys. Lett. B **463**, 339 (1999).

[80] P. L. Anthony *et al.*, Phys. Lett. B **458**, 529 (1999).

[81] P. L. Anthony *et al.*, Phys. Lett. B **553**, 18 (2003).

[82] K. Ackerstaff *et al.*, Phys. Lett. B **404**, 383 (1997).

[83] A. Airapetian *et al.*, Phys. Rev. D **75**, 012007 (2007).

[84] A. Airapetian *et al.*, Eur. Phys. J. C **72**, 1921 (2012).

[85] X. Zheng *et al.*, Phys. Rev. Lett. **92**, 012004 (2004); Phys. Rev. C **70**, 065207 (2004).

[86] S. E. Kuhn, J.-P. Chen and E. Leader, Prog. Part. Nucl. Phys. **63**, 1 (2009).

[87] O. A. Rondon, EPJ Web Conf. **73**, 02001 (2014).

[88] E. Leader, A. V. Sidorov and D. B. Stamenov, Phys. Rev. D **84**, 014002 (2011).

[89] E. Leader, A. V. Sidorov and D. B. Stamenov, Phys. Rev. D **91**, 054017 (2015).

[90] M. Göckeler, R. Horsley, D. Pleiter, P. E. L. Rakow, A. Schafer, G. Schierholz, H. Stuben and J. M. Zanotti, Phys. Rev. D **72**, 054507 (2005).

[91] F. R. Wesselmann *et al.*, Phys. Rev. Lett. **98**, 132003 (2007).

[92] K. Slifer *et al.*, Phys. Rev. Lett. **105**, 101601 (2010).

[93] W. Melnitchouk, R. Ent and C. Keppel, Phys. Rep. **406**, 127 (2005).

[94] Jefferson Lab Experiment E12-06-121, T. Averett, B. Sawatzky, W. Korsch and Z.-E. Meziani, spokespersons.

[95] Jefferson Lab Experiment E12-06-110, J.-P. Chen *et al.*, spokespersons.

[96] Jefferson Lab Experiment E12-06-122, B. Wojtsekhowski *et al.*, spokespersons.

[97] The Jefferson Lab Angular Momentum (JAM) Collaboration website, `http://www.jlab.org/JAM`.